

Machine learning based nowcasting of the Vögelsberg deep-seated landslide: why predicting slow deformation is not so easy

Adriaan van Natijne¹, Thom Bogaard², Thomas Zieher³, Jan Pfeiffer³, and Roderik Lindenbergh¹

¹Department of Geoscience & Remote Sensing, Faculty of Civil Engineering and Geosciences, Delft University of Technology, Delft, the Netherlands

²Department of Water Management, Faculty of Civil Engineering and Geosciences, Delft University of Technology, Delft, the Netherlands

³Institute for Interdisciplinary Mountain Research, Austrian Academy of Sciences, Innrain 25, 6020 Innsbruck, Austria

Correspondence: Adriaan van Natijne (A.L.vanNatijne@tudelft.nl)

Abstract.

Landslides are one of the major weather related geohazards. To assess their potential impact and design mitigation solutions, a detailed understanding of the slope processes is required. Landslide modelling is typically based on data-rich geomechanical models. Recently, machine learning has shown promising results in modelling a variety of processes. Furthermore, slope conditions are now also monitored from space, in wide-area repeat surveys from satellites. In the present study we tested if use of machine learning, combined with readily-available remote sensing data, allows us to build a deformation nowcasting model. A successful landslide deformation nowcast, based on remote sensing data and machine learning, would demonstrate effective understanding of the slope processes, even in the absence of physical modelling. We tested our methodology on the Vögelsberg, a deep-seated landslide near Innsbruck, Austria. Our results show that the formulation of such a machine learning system is not as straightforward as often hoped for. The primary issue is the freedom of the model compared to the number of acceleration events in the time series available for training, as well as inherent limitations of the standard quality metrics such as the mean squared error. Satellite remote sensing has the potential to provide longer time series, over wide areas. However, although longer time series of deformation and slope conditions are clearly beneficial for machine learning based analyses, the present study shows the importance of the training data quality but also that this technique is mostly applicable to the well-monitored, more dynamic deforming landslides.

1 Introduction

Landslides make up for 6% of the weather related disasters globally (WMO, 2019). To protect the public, landslides have been a major research topic for the last decades. For local landslide mitigation by geotechnical intervention an up-to-date understanding of these hydro-meteorological phenomena, their feedbacks and impact is desired. This understanding may then be leveraged for the design of landslide hazard mitigation measures.

Where the installation of effective remediation concepts is not possible, early warning systems may help to reduce the landslide risk. Such systems should quickly adapt to changing conditions, both on the slope and ~~global~~ globally (e.g. climate change). Moreover, such a system should be fast to adapt and implement to assess as many slopes as possible.

Existing local systems typically provide early warning based on in-situ slope monitoring (Guzzetti et al., 2020). An example of
25 a satellite based, global early warning system is the LHASA model (Kirschbaum and Stanley, 2018; Hartke et al., 2020; Stanley
et al., 2021) that provides a global nowcast of acute landslide susceptibility. However, these systems typically focus on sudden,
fast, and shallow landslides. Literature reports mixed success in the replacement of local measurements by satellite observations
for the prediction of shallow landslide collapse (Thomas et al., 2019; Yatheendradas et al., 2019). Such catastrophic events
change the landscape, and as a consequence the situation before and after the collapse are no longer comparable. Therefore,
30 the landslide process preceding the collapse can only be studied if data from before the landslide is available.

We focus on slow moving, reactivating, deep-seated landslides on natural slopes, for which the deformation pattern is controlled
by hydro-meteorological forcing. These deep-seated landslides are estimated to comprise 50% of the landslides globally (Her-
rera et al., 2018; Novellino et al., 2021). The deep-seated landslides we focus on rarely evolve into catastrophic collapse and
often entail a complex response to hydro-meteorological conditions controlling the landslide's pore pressure (Bogaard and
35 Greco, 2015). They are characterised by gradual, non-catastrophic deformations that can be responsible for extensive infras-
structure damage (Mansour et al., 2011). Deformation rates typically vary from millimeters to decimeters per year, whereas
phases of acceleration or deceleration often correlate with time-delayed hydrological conditions (Intrieri et al., 2018).

Monitoring systems only supported by the detection of currently emerging acceleration events (e.g. Carlà et al., 2017), can only
be used to detect already ongoing acceleration. As a consequence, adequate early warning is only possible if the deformation
40 can accurately be predicted beforehand. Therefore, the deformation should be predicted from the predisposing conditions on
the slope, combined with dynamic factors such as infiltrating precipitation and snowmelt that lead to higher pore pressures,
instability and subsequent deformation. However, the deformation behaviour of such slow, deep-seated landslides is 'extremely
difficult' to model (Van Asch et al., 2007).

Past landslide deformation events are indicative of the future behaviour, as landslides are likely to display similar behaviour
45 in similar situations (Fell et al., 2008; Guzzetti et al., 1999). Unlike catastrophic landslides, where the landslide dynamics
change permanently, slow moving landslides are not single, catastrophic incidents. Therefore, analysis of the monitoring data
of deep-seated landslides is expected to reveal causal factors in landslide deformation, which allow for a continuous cycle of
forecast and validation of the relationship between deformation and the conditions on the slope.

Deformation nowcasting could be considered an intermediate option between monitoring and modelling, integrating sensor
50 data to estimate the current situation (the system state) and extrapolate on a short timescale. New data and data integration
methods, 'machine learning', offer new possibilities for such data-driven landslide forecasting (van Natijne et al., 2020). Fur-
thermore, these techniques offer new capabilities to continuously track the system state without extensive, in-situ sensor net-

works and physics-based modeling. Such data-driven models could be used to ‘learn’ the landslide dynamics and the interplay of hydro-meteorological factors from the deformation signal of the landslide.

55 In the last decades satellite observations have increased in quantity, shortening the time between subsequent acquisitions, as well as increasing the variables observed (Belward and Skøien, 2015). These acquisitions provide us with a global overview of the status of the earth at local scale, often with weekly to daily updates. More recently there is the tendency to make the data freely available, a development that lowered the barrier for innovations (Zhu et al., 2019), and especially benefits experiments that require long time series, like this study. Even though their coverage is often limited to the surface, and the spatial resolution
60 (often kilometer range) lacks the details of close-range measurements, the repeated monitoring of the slope conditions may still reveal the slope processes responsible for accelerated deformation (van Natijne et al., 2020).

Here we present a data-driven nowcasting model with a four day lead time of the deformation of the Vögelsberg landslide, near Innsbruck, Austria. We use readily available, remotely sensed data and products, and test various similar remote sensing products to assess their relative performance in the nowcasting model. We discuss the complications encountered during modelling:
65 over-parametrization, the impact of optimization metrics, and the challenges due to the deep-seated landslide inertia compared to the highly dynamic forcing of the slope.

First, we introduce the modelling options, and study area. Second, we present the resources available to us, and our modelling approach, followed by the results and an extensive discussion on the insights gained during the modelling exercise. Last, we provide recommendations for future data-driven landslide nowcasting exercises.

70 **2 Data-driven modelling approaches**

In the present study we interpret data-driven modeling as a form of naive modelling. That is, the model is unaware of the physics behind the landslide process. For data-driven models, the deformation of the slope is merely a signal to be reproduced from a collection of observations by empirical relations, in contrast to traditional, landslide geomechanical modelling, that is rooted in physics. Table C1 features a selection of studies into data-driven deep-seated landslide nowcasting, demonstrating the
75 recent interest in this topic. Various examples come from landslides around the Three Gorges Dam that are strongly controlled by the reservoir water level (e.g., Yang et al. (2019)). However, this is not the most common type of deep-seated landslide. Deep-seated landslide deformation is typically driven by ~~the~~ water storage in the deeper subsurface, ~~that~~. This storage is controlled by a long-term water balance of precipitation and snowmelt input, evaporation losses ~~;~~ and regional groundwater ~~input and drainage exchange~~ (Bogaard and Greco, 2015). Other approaches split the deformation into a trend and predict the
80 smaller trend deviations using a complex machine learning approach (e.g., Miao et al. (2022)), although in our view the trend is an integral part of the deformation signal to be predicted.

The indirect transfer from precipitation and snowmelt to storage may be captured by, for example, including recent observations in a bucket model (Nie et al., 2017). A bucket model represents the subsoil as a storage that is replenished by precipitation and emptied by drainage and evaporation. Furthermore, changes to the storage may involve a time delay, depending on complex

85 infiltration processes. This process may be dependent on the precipitation type, duration and intensity. Moreover, deformation may not be governed by a short and single precipitation event. For example, a short, extreme precipitation event or three days of consecutive drizzle may introduce similar amounts of water to the system, but will be represented differently in storage changes due to different infiltration abilities of the soil. All in all, modelling of deep-seated landslides will likely require some form of storage modelling, where these dynamics are either resolved by the model or in advance by an expert.

90 Two distinct modelling approaches can be distinguished. Modelling is either based on classification of the environmental conditions and associated deformation response, or calculates the expected deformation response from the conditions on the slope. In either case the model parameters are tuned on historic observations such that they best reproduce the deformation signal from the conditions observed previously at the slope. Our model of the Vögelsberg landslide is a continuous model. For completeness classification models will be introduced briefly.

95 **2.1 Classification models**

Based on the assumption that similar conditions trigger a comparable deformation response (Fell et al., 2008; Guzzetti et al., 1999), conditions and responses may be categorized. The current slope conditions are then matched against historic conditions, and the deformation response is assumed to be the same. Extrapolation of the response to previously unencountered conditions is typically impossible with these models. However, the system will therefore also not yield unrealistic results, and could be
100 considered bound to the previously encountered deformation signal.

2.2 Continuous models

The simplest, linear, model is the weighted sum of the quantified conditions at the slope. However, the slope response may not be linear and is typically not immediate. Neural networks may be used to estimate any signal by the formation of a network of interlinked nodes that ingest and combine the conditions on the slope in subsequent layers of nodes (Hornik et al.,
105 1989; Hill et al., 1994). A time series passed to a single input neuron is equal to a weighted sum of the time series, plus a bias.

As more hidden layers of neurons are introduced to the system, the direct link to the (time series) input is lost, as combinations are made. Furthermore, an activation function may be applied to scale the output of each node, especially to normalize the response and filter outliers, at the cost of introducing non-linearity to the system. The number of parameters, degrees of freedom of the model, are associated with the number of input variables. When historic observations are supplied as additional
110 observations, they will each require their own model parameters, and increase the degrees of freedom in the model.

State aware models, such as Recurrent Neural Networks (Connor et al., 1994), maintain a track record of the state of the landslide instead, and iterate over the input time series in successive model runs. Individual observations are fed into the system, with the system maintaining track of their contribution to the current state of the landslide. These models resemble a bucket model, a simplified representation of the water storage in the subsoil. However, unlike in a traditional (soil moisture/ground
115 water) bucket model, all variables are taken into account, even if they do not directly represent water. Furthermore, unlike

regular neural networks, the number of trainable parameters is not dependent on the length of the history supplied to the model, but on the number of memory cells and time series.

Models based on Recurrent Neural Networks suffer from computational difficulties during optimisation, where gradients may vanish (Bengio et al., 1994; Hochreiter and Schmidhuber, 1997; Hochreiter, 1998). Therefore, they are typically replaced by
120 models based on Long Short-Term Memory (LSTM) nodes (Hochreiter and Schmidhuber, 1997), that do not suffer from this due to built-in normalisation. Each LSTM ‘bucket’ is capable of weighting, retaining and clearing a memory of previous inputs, and as such tracks the system state.

The challenge specific to forecasting and nowcasting is the absence of information on the future slope conditions. The latest information available to the system are the current conditions and the last estimation of the system state. Auto-regressive models
125 predict these conditions as well, so that subsequent forecasts may use these environmental conditions in their models. However, especially precipitation is governed by external influences and may not be predictable from the other forcing parameters in the system. As an alternative, forecasts may be included into the model. However, this would require forecasts for all input variables. Therefore, such system was deemed not suitable for this application.

Special attention should be paid to the robustness of the model. Even ten years of daily observations will result [in](#) a time series
130 of less than 4 000 reference observations, much less than desirable for use in more complex machine learning models such as neural networks (Cerqueira et al., 2019). If too few training data are provided, the abundance of input data creates unique combinations of conditions and outputs. This will lead to excellent performance during training, but reduced performance during testing and application, and is known as over-fitting.

There are infinite data-driven modelling possibilities and the generic character of many data-driven models suits the diversity
135 in available remote sensing variables. However, due to the limited length of the time series, in comparison to typical machine learning studies, one should stay close to the physics and processes, to limit the freedom of the model towards a solution. Therefore, one has to ensure a balance between the number of parameters to be estimated and the training/validation data available.

3 Case study: the Vögelsberg landslide

140 The Vögelsberg is a deep-seated landslide, located in the Wattens basin, near Innsbruck, Austria (Figure 1). Its north-east facing slope covers approximately 4.6 km², and ranges between 750 m and 2200 m above sea level. A nearby weather station reports an average yearly precipitation of 896 mm, of which 13% is in the form of snow. The lower, active part of the landslide is only about 0.2 km² and is covered by pasture fields, sparse forests and few houses and farm buildings. The shearzone was identified via inclinometer measurements to be at 43–51 m below the surface, although strongly disintegrated soil up to 52–70 m indicates
145 a long history of activity (Pfeiffer et al., 2021).

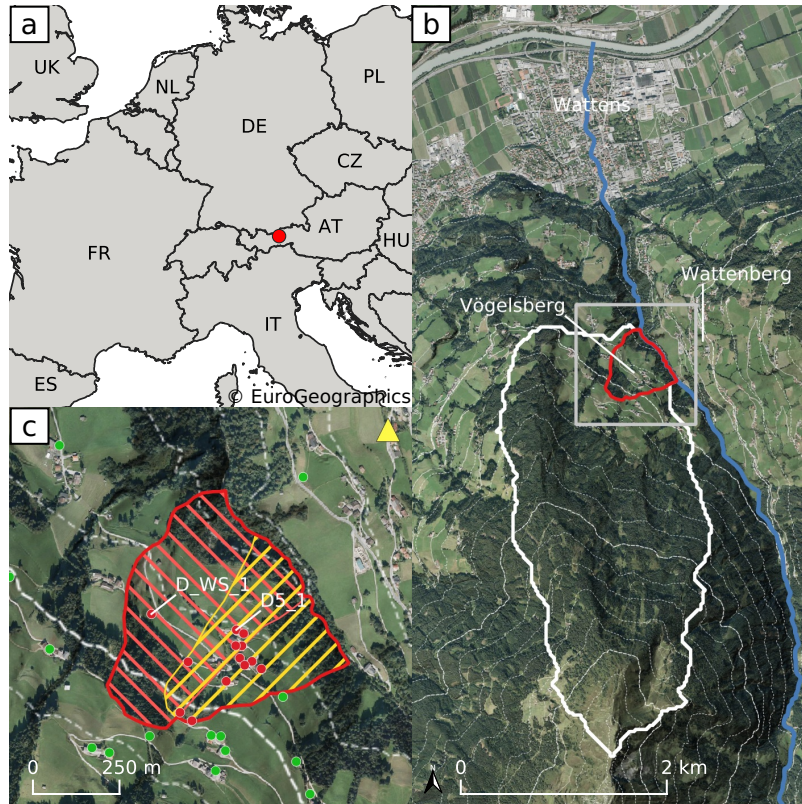


Figure 1. a) Location of Vögelsberg in Europe. b) Overview of the landslide catchment (white) and active region of the Vögelsberg landslide (red). Dashed contour lines are shown every 100 meters of elevation change. The coverage of sub-figure c) is indicated in gray. c) Detail of the active region of the Vögelsberg landslide. The northern subsection of the slope (red) and southern (yellow) section and overlapping area are marked. Out of a total 53 retroreflecting prisms, the 29 benchmarks with the longest time series (2016–2020) are shown. Benchmarks on the landslide are shown in red, stable, reference benchmarks in green. The time series of benchmarks ‘D_WS_1’ and ‘D5_1’ are shown in Figure 2. The location of the total station in Wattenberg is marked by a yellow triangle. (Backgrounds: Eurostat/[EuroGeoGraphics](#)/[EuroGeoGraphics](#); Federal State of Tyrol, Austria)

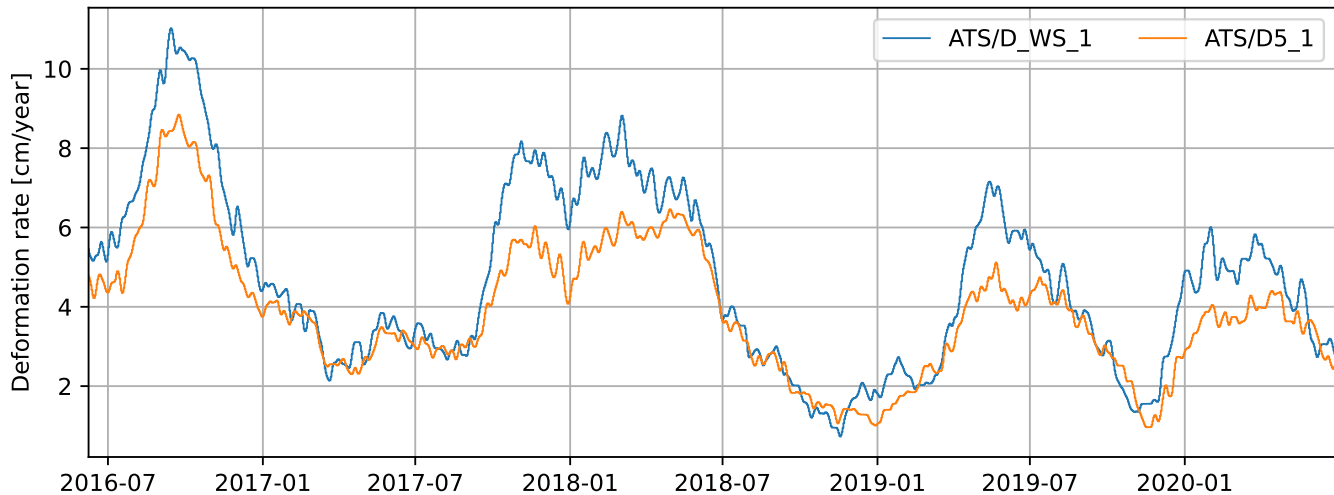


Figure 2. Daily deformation rate of the Vögelsberg landslide at benchmarks ‘D5_1’ and ‘D_WS_1’ (Figure 1), as measured by the automated total station and smoothed by a moving average filter over the last 32-days.

In 2016 a Leica TC1800 Automated Total Station (ATS) was installed in Wattenberg, opposite to Vögelsberg, by the Division of Geoinformation of the Federal State of Tyrol. The system surveyed each of the fifty-three benchmarks every hour. Extensive corrections to the measurements were necessary, primarily due to the instability of the monument the total station is located on. In this study a series of pre-processed range measurements was used, fixed to stable benchmarks around the active area that showed no signs of landslide deformation damage. The accuracy of this time series was estimated to be in the order of ± 0.54 cm/a (Pfeiffer et al., 2021). The time series of the displacement rate at the two benchmarks used in this study are shown in Figure 2, their locations are indicated in Figure 1. Time series of the other benchmarks are shown in Pfeiffer et al. (2021, Figure 3) [Figure 3 of Pfeiffer et al. \(2021\)](#).

The deformation of the Vögelsberg landslide is a complex response to the hydro-meteorological conditions in the catchment, in particular precipitation and (delayed) infiltration from snowmelt. A binary prediction of stability/instability or acceleration/deceleration is insufficient for the Vögelsberg landslide, as the slope is undergoing continuous deformation. Pfeiffer et al. (2021) conducted a full, [in-situ](#) assessment of the hydro-meteorological drivers and found a 20–60 day time lag between rainfall and acceleration and a 0–8 day time lag between snowmelt and acceleration. Noteworthy is the difference in behaviour between the northern and southern sections of the slope, represented by benchmarks ‘D_WS_1’ and ‘D5_1’ respectively (Figure 2). The northern section of the slope (‘D_WS_1’) shows a higher variability in the deformation signal, with stronger accelerations than the southern, inhabited section of the slope (‘D5_1’). We focus on these two benchmarks, as a balanced representation of the two landslide sub-systems.

The deformation rate, derived from the total station range measurements, was smoothed by a moving average filter until few, noise induced, negative (up-slope) deformations remained, while maintaining the highest possible temporal resolution

165 (Figure B1). Only historic observations may be used in an operational early warning system, and a moving average of the most recent 32 days was necessary to remove most of the noise. As a consequence, the onset of acceleration will be only 1/32 of the signal and thus severely dampened, stressing the need for an acceleration prediction rather than extrapolation of deformation measurements as warning signal. Moreover, signals shorter than the filter length will be reduced in amplitude.

4 Methodology

170 Our model's aim is to predict the landslide deformation based solely on the current conditions at the slope. No recent deformation observations or prior defined geomechanical model will be available to our model during prediction. The main model constraints are that we have a relatively limited amount of data points (1 482 samples) and will work with readily available remote sensing data and products. Furthermore, we set the objective to model with daily time steps and a forecast lead time of four days. A successful prediction of the deformation rate four days ahead will demonstrate the model's ability to predict a
175 tipping point based on the environmental conditions (acceleration, peak, deceleration). Moreover, a four day prediction would give sufficient time for further investigation as part of an early warning system.

With these constraints in mind, a system was designed based on a parsimonious recurrent neural network. First, we will introduce the data available. Second, an overview is provided of the pre-processing applied to the input variables. Third, we provide the specifications of our model. Last, the training and validation of the model are discussed.

180 4.1 Model variables

The model variable selection is based on the analysis of factors of influence (Pfeiffer et al., 2021), and are mainly of data-driven nature. Pre-disposing or causal factors, such as topography, that are necessary for a landslide to form, are considered static in this study. Therefore, the focus is on the dynamic conditions leading up to landslide instability and deformation, and triggering factors. The selection of variables is listed in Table 1.

185 Our method is designed with the intent to be generally applicable. Therefore, ~~where possible~~except for the deformation, remote sensing products were used, as they are likely to be available elsewhere as well. Where available, redundant products, that represent the same or similar quantities, were included to assess their relative performance in the nowcasting model. The correlation between the products is limited ($\mu_{|\rho|} = 0.16$, $\max|\rho| = 0.7$, Figure A1), indicating differences between the products of the same quantity. Effects that may not be observed directly, such as soil moisture under snow, require some form of
190 modelling or re-analysis. These quantities, not directly available from remote sensing, are taken from re-analysis models 'ECMWF Re-Analysis, version 5' (ERA5) and the 'Global Land Evaporation Amsterdam Model' (GLEAM).

The desired output of our model is a daily, four days ahead prediction of the landslide deformation rate at benchmarks 'D_WS_1' and 'D5_1'. Reference, training and validation samples are provided by the automated total station located on the Wattenberg, opposite to Vögelsberg (Figure 1). Deformation measurements were performed hourly from 2016-05-04 to
195 2020-06-28, and aggregated to 1 482 daily averages to reduce noise. The noise in the signal was further reduced by a 32-day

Table 1. Selection of time series considered for integration into the model. Deformation variables are marked ‘D’, while slope conditions, input variables to the model, are marked ‘V’. Observations are marked ‘S’ for directly observed variables processed and available within the time frame of a nowcasting system; ‘R’ for re-analysis variables, and ‘M’ for variables modelled within this study (see §4.2). References to the various sources are provided in the main text. The internal identification is derived from the variable as referenced by the source, and is used throughout the figures to refer to the various time series. From rasterized products, only the time series closest to Vögelsberg was used.

| | Variable | Source | Type | Spatial res. | Temp. res. | Int. identification |
|-----|-----------------------------|-------------|----------------|-------------------------|------------|----------------------|
| D1 | Deformation ‘D_WS_1’ | ATS (local) | S | point | daily | ATS/D_WS_1 |
| D2 | Deformation ‘D5_1’ | ATS (local) | S | point | daily | ATS/D5_1 |
| V1 | Precipitation | ERA5 | R | 0.1° (\simeq 10 km) | hourly | ERA5/tp |
| V2 | Precipitation | GPM | S | 0.1° (\simeq 10 km) | 30 min. | GPM/precipitationCal |
| V3 | Snow water equivalent | ERA5 | R | 0.1° (\simeq 10 km) | hourly | ERA5/swe |
| V4 | Snowmelt | ERA5 | R | 0.1° (\simeq 10 km) | hourly | ERA5/smlt |
| V5 | Soil moisture, full profile | SMAP | S R | 0.1° (\simeq 10 km) | 3 hrs. | SMAP/sm_profile |
| V6 | Soil moisture, root zone | GLEAM | R | 0.25° (\simeq 25 km) | daily | GLEAM/SMroot |
| V7 | Soil moisture, 100–289 cm | ERA5 | R | 0.1° (\simeq 10 km) | hourly | ERA5/swv14 |
| V8 | Evaporation | GLEAM | R | 0.25° (\simeq 25 km) | daily | GLEAM/E |
| V9 | Air temperature | ERA5 | R | 0.1° (\simeq 10 km) | hourly | ERA5/t2m |
| V10 | API | | M | point | daily | API/API |
| V11 | Sesonal noise | | M | point | daily | fake/fake |

moving average filter, of which the results are shown in Figure 2. The time series at the 51 other benchmarks (Figure 1) were not used in the modelling.

Daily precipitation information is provided by the Integrated Multi-satellitE Retrievals for GPM (IMERG) algorithm of the Global Precipitation Measurement mission (GPM) (NASA, 2018). ‘Early’ results are provided with sub-day delay, and are therefore especially suitable for an operational nowcasting model. For comparison daily precipitation from the ECMWF ERA5 Land re-analysis is included as well (ERA5, 2019). Snow properties are covered by two products of the ERA5 Land re-analysis: snow water equivalent, and snowmelt.

Soil moisture, especially at depth, cannot be observed directly from space at a high enough resolution for this application. The [low latency](#) operational products from the Copernicus Land Service, Soil Water Index and Surface Soil Moisture, are frequently unavailable either due to unfavourable slope topography or due to snow cover. Alternatives are provided by SMAP ([Entekhabi et al., 2010](#)); a re-analysis from [L4](#) ([Entekhabi et al., 2010](#); [Reichle et al., 2022](#)); ‘Global Land Evaporation Amsterdam Model’ (GLEAM) (Martens et al., 2017; Miralles et al., 2011); and ERA5 Land (ERA5, 2019). Evaporation estimates

are taken from GLEAM as well. Air temperature, a proxy indicator of evaporation and snowmelt, is included from ERA5 Land (ERA5, 2019).

210 4.2 Variable preparation

The model is fed with the eleven variables defined in §4.1 (Table 1). Except for the deformation time series, all sources consist of gridded products, with wide area coverage. In this study only the data point closest to the active part of the Vögelsberg landslide was used. To match the time resolution of the deformation measurements the model is run at daily intervals. Observations available at shorter intervals are aggregated to daily means first. Where data is missing, for example due to sensor failure, 215 the values are filled with the data from the previous day (forward filling), as would be possible in an operational scenario. Furthermore, two modelled time series were added to the system: an antecedent precipitation index (API) as basic hydrological model and a random, seasonal noise signal.

The Antecedent Precipitation Index (API, $API / API, V10$) was designed to estimate the water present in the watershed (Kohler and Linsley, 1951; Heggen, 2001). The API is included to determine if such variable could support the deformation nowcasting 220 model. Precipitation less than 0.1 mm was ignored, in addition a 10% direct evaporation loss, and a 4% daily storage loss is assumed. These parameters were chosen based on an [expert's estimate of the hydrological setting by an experienced landslide hydrologist](#). The API at time step t is calculated as

$$API_t = \max(0, p - 0.1) \cdot 0.9 + 0.96 \cdot API_{t-1}, \quad (1)$$

with p the daily precipitation sum. The API, calculated from the operational GPM precipitation data (GPM/precipitati- 225 onCal), is shown in Figure 3.

A random variable with seasonal characteristics is added to the variable selection to analyze the effect of spurious correlation on the model. The random variable, $fake / fake (V11)$, based on Brownian motion, is tuned to match a typical seasonal characteristic in the 32-day history relevant to the model. The auto-correlation behaviour is illustrated in Figure 4, and resembles the dynamics of both the surface temperature as provided by ERA5 and the soil moisture from SMAP for the first 2–3 months. 230 Longer correlation periods are not relevant for our model.

All variables are offset to become zero-mean and scaled by the standard deviation. Therefore, all input variables are on approximately equal scale and represented as deviations from their average condition. The normalization parameters, mean and standard deviation, should be kept fixed while new data is added, to remain consistent with the scaling of the time series used during training. The data set is fed to the model as a time stamped collection of daily observations, illustrated in Figure 3.

235 4.3 Model configuration

Our model is a shallow neural network with only a single hidden layer (Jain et al., 1996). This hidden layer consists of a single Long Short-Term Memory (LSTM) node (Hochreiter and Schmidhuber, 1997), that resembles a bucket model for the water storage in the subsoil. The model is supplied with a thirty-two day history of observations, equal to the length of the moving

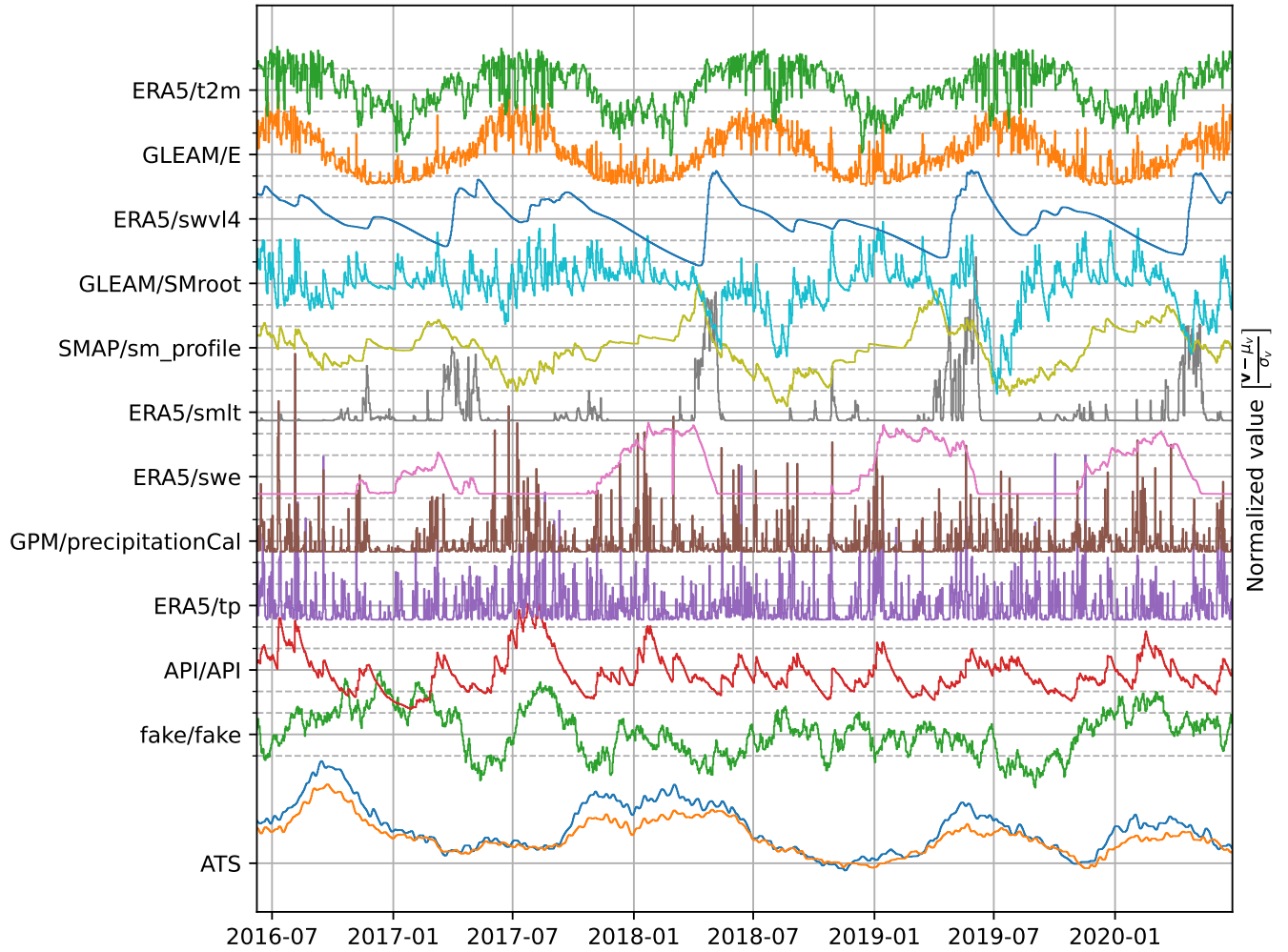


Figure 3. Overview of the variable space (Table 1). The values are offset to a zero mean and scaled by their standard deviation. A single iteration of the seasonal noise ($f_{\text{fake}}/f_{\text{fake}}$) is shown as an example.

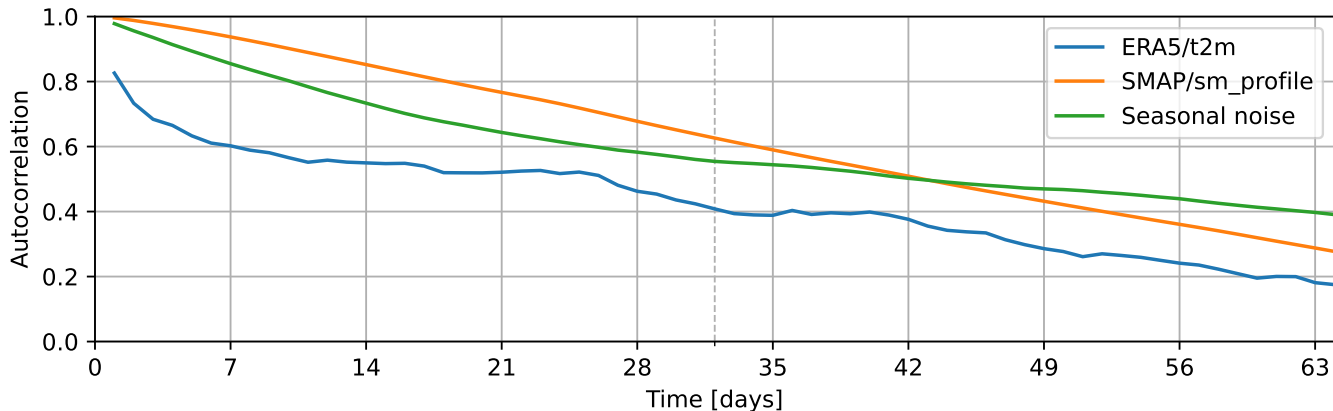


Figure 4. Autocorrelation of one of the generated signals compared to the autocorrelation of the temperature as taken from ERA5 (ERA5/t2m) and the soil moisture estimate from SMAP (SMAP/sm_profile). The length of the history as used by the model, 32 days, is indicated by the dashed line.

average filter, longer than the lag time for snow (0–8 days) and sufficient to cover most of the 20–60 day lag time for rainfall
 240 at the Vögelsberg landslide found by Pfeiffer et al. (2021). From a pre-defined, optimized initialisation, the model is cycled
 for each day of preceding observations, feeding the observations into memory, before a prediction is made based on the final
 bucket values (\mathbf{m}). The model is illustrated in Figure 5, as function of environmental conditions (\mathbf{x} , Table 1), at each of the
 $n = 32$ days preceding the nowcast, the LSTM node and four neurons of a single benchmark, one for each prediction day. This
 last, output, layer is repeated for both benchmarks (‘D_WS_1’ and ‘D5_1’) to be predicted, while the LSTM memory (\mathbf{m}) is
 245 shared between the benchmarks to reduce the number of parameters.

In total, for a network configuration with a single memory cell (\mathbf{m}), 68 parameters have to be estimated. The LSTM node, with
 one hidden state, requires 52 parameters to be estimated for the eleven variables (Table 1). Sixteen parameters are required for
 the output, eight for each of the deformation time series: one bias and one scaling parameter per day for the final state of the
 LSTM node. The number of parameters to be estimated is independent of the history length.

250 Four parameters are added per extra prediction day (two benchmarks, one bias and weight each). An extra memory cell requires
 $8h + 4x + 1$ extra parameters, with h the current number of hidden nodes and x the number of input variables. While only four
 parameters are added for each additional input variable. Hence, extra memory always requires more parameters than extra
 input variables. Therefore, to limit the number of parameters in the model and minimize the risk of over-fitting, the addition of
 a variable to the model should be preferred over the addition of a memory cell.

255 An interpretation of the network is that the development of the slope state in the last 32-days is described by the LSTM
 node. The state is scaled, and otherwise matched to the individual benchmarks, by the output neurons. The four days are an
 extrapolation of the current state of the system, no prediction of the conditions on the slope is made.

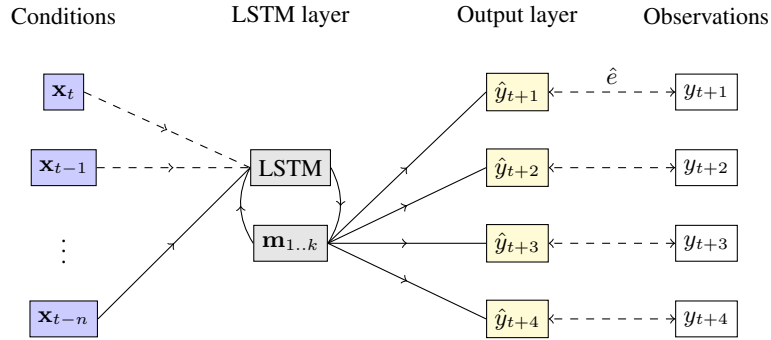


Figure 5. Simplified schematic of the model. From left to right: the hydro-meteorological conditions (\mathbf{x}_t) on the slope at the current (t) and n preceding time steps; the LSTM layer, including its internal feedback and memory cells ($\mathbf{m}_{1..k}$); the output layer \hat{y}_t , which combines the k memory-cells \mathbf{m} of the LSTM node to four predictions; the observations y_t , as available for comparison during training and validation. During initialisation, the conditions on the slope are fed to the system on a day-by-day basis, starting at the oldest observations. The output layer is only invoked at the last iteration, with the final values of the LSTM memory. The parameters of the LSTM layer are optimized on both deformation time series in parallel, the output nodes are tuned individually for each benchmark.

The ‘mean squared error’ was chosen as the loss function. This function, that quantifies the difference between the predicted and observed deformation, is to be minimized during training. The quality of the prediction is measured on the period not used
 260 for training. This function assures the cumulative deformation over time is realistic, as errors are balanced between over- and underestimation. Therefore, the predictions will not show a bias towards acceleration or deceleration.

The TensorFlow machine learning framework was chosen to implement the model (Google, 2022). The LSTM model is implemented in a stateless fashion: the warm-up phase is repeated for every nowcast. The model was run on a workstation based on an Intel Xeon W-2123 (4 cores, 8 threads, 3.6 GHz) with 32 GB RAM, while model variations were tested on the high
 265 performance computing cluster of the Delft University of Technology. Given the limited size of the region of interest, as well as the limited number of parameters, the full model fits into 1 GB of memory.

4.4 Model training & validation

During training the model parameters are tuned such that the final model state best describes the deformation prediction. The model is optimized with the Adam optimizer (Kingma and Ba, 2017). The model is trained on the loss, after 50 training passes
 270 that do not lower the mean squared error over the training period, the model’s parameters are fixed. If this steady state is not achieved after 25 000 passes, the training is stopped anyway and the model parameters used as-is.

Due to temporal correlation training and validation cannot be divided over random chunks or batches, according to the ‘traditional’ 30%–70% chunks (Gholamy et al., 2018). Therefore, the training data is split into equal years instead, as shown in
 275 Figure 6. Data outside the training period is used for validation. This includes the period before the training period, when available.

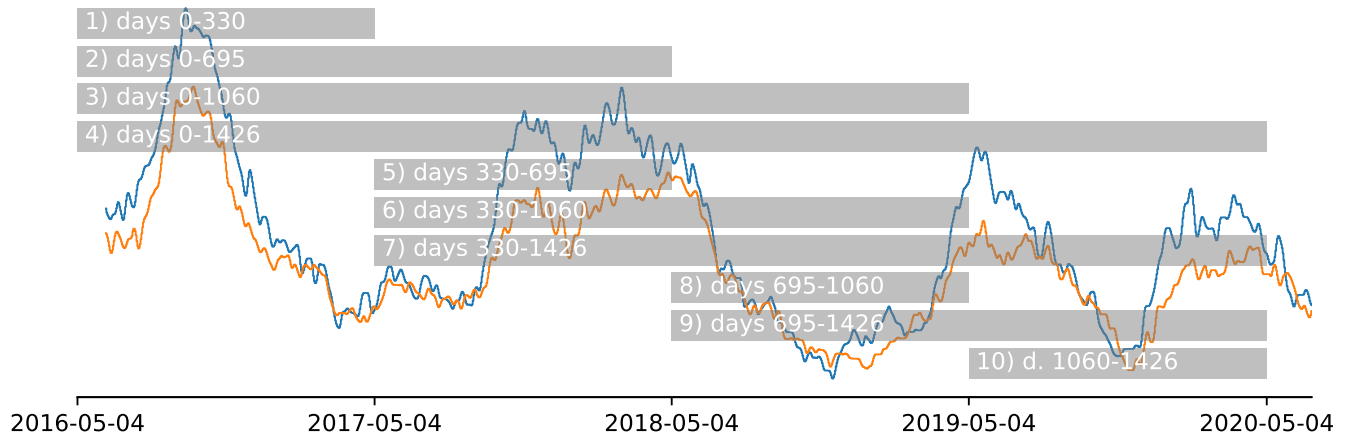


Figure 6. Training periods as supplied to the model. The data outside the training period is used for validation. Note that with the longest training period (4), there is very limited validation data left. The deformation pattern (Figure 2) is shown in the background for reference. As there is no clear seasonality in the deformation signal, the data set was split in approximate years from the start of the measurements.

The robustness of the model to the selection of the training data is assessed from the stability of the results when training over the subsequent periods (Figure 6), a variation on cross-validation (Krkač et al., 2020). Each model iteration starts with the same (random) initial weights, but is trained independently from the start. The quality of fit is assessed by evaluation of the loss function, the mean squared error, on the periods not used for training. Finally, the model performance is compared between the training periods. Large deviations of the model quality suggest there are dynamics the system is not capable of describing.

To assess the impact of irrelevant data on the system, as well as the effect of over-fitting, the additional, correlated random variable (*fake/fake*) is used. Over-fitting will make the model prone to spurious correlation with this variable, that results in poor performance in the validation stage. Furthermore, to ensure there is no accidental correlation between the seasonal noise and the deformation signal during training and/or validation, the signal was re-rendered for every model run.

All possible combinations of the eleven input variables were tested on the model. With eleven variables this results in $2^{11} - 1 = 2047$ combinations, as each of the time series may be used or not (2 options), except for the case where no input is used. Furthermore, the model was trained and validated on each of the ten combinations of training and validation year(s). Each sequence of model training and validation was repeated at least three times, to account for the ‘luck’ introduced by the random initialization of each model. In total 147 984 model runs were performed.

5 Results

The best solution out of all model runs, judged on the minimal mean squared error on validation, is based on a single LSTM-node and only four of the eleven input variables available: precipitation from GPM (V2); soil moisture from SMAP (V5) and

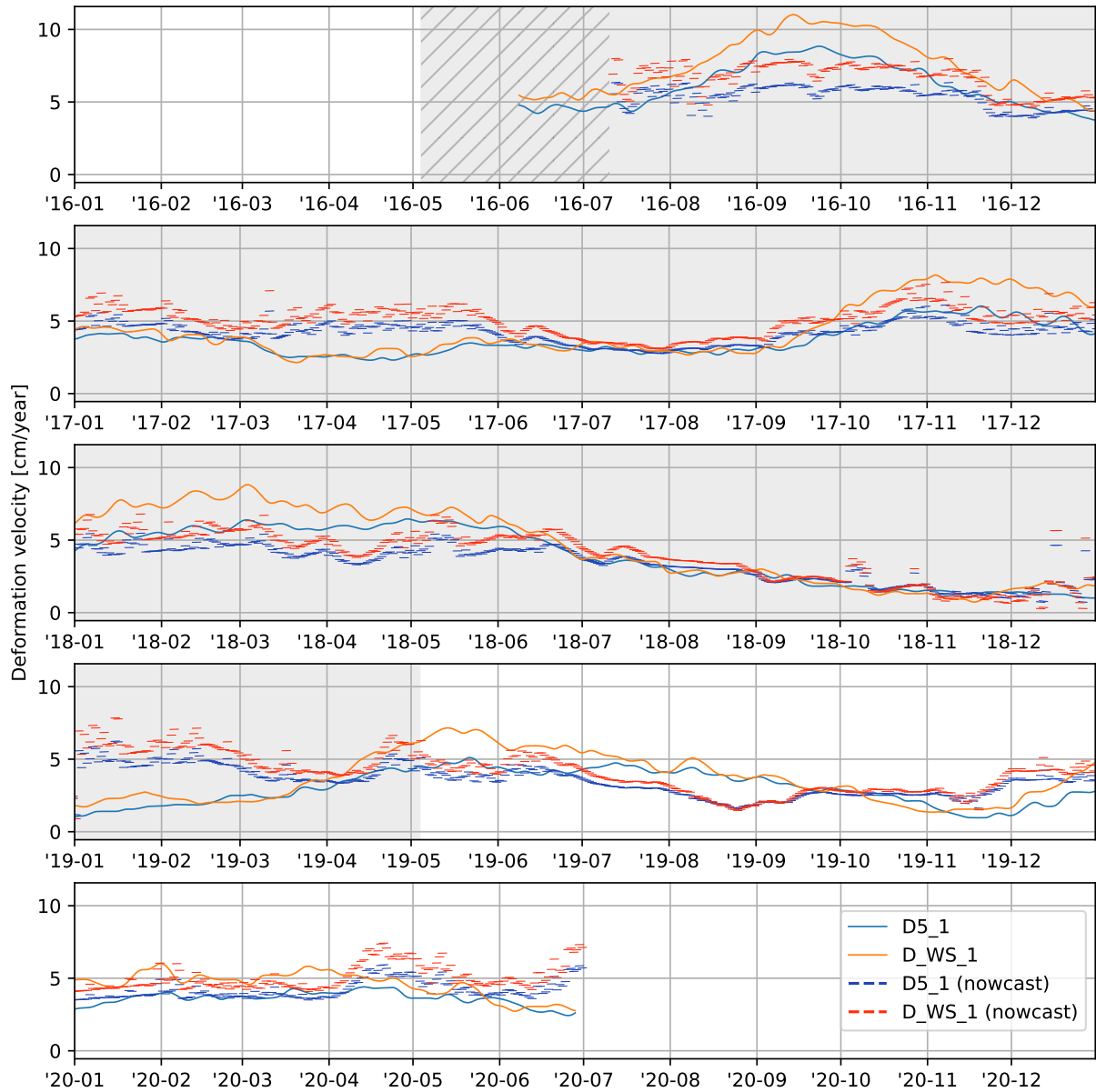


Figure 7. Result of the deformation nowcast, run of the full time frame of the available deformation time series. The shaded time span was used for training. Shown as thin lines are the subsequent, daily, nowcasts for benchmarks 'D5_1' and 'D_WS_1'. Per day four deformation nowcasts are shown, with the start of each line being the day after the day the nowcast was issued. Note the warm-up time at the start, shown hatched and without predictions, that is required to initialize the moving average filter on the deformation data and fill the memory of the LSTM-node. The final nowcast ends four days after the end of the reference measurements.

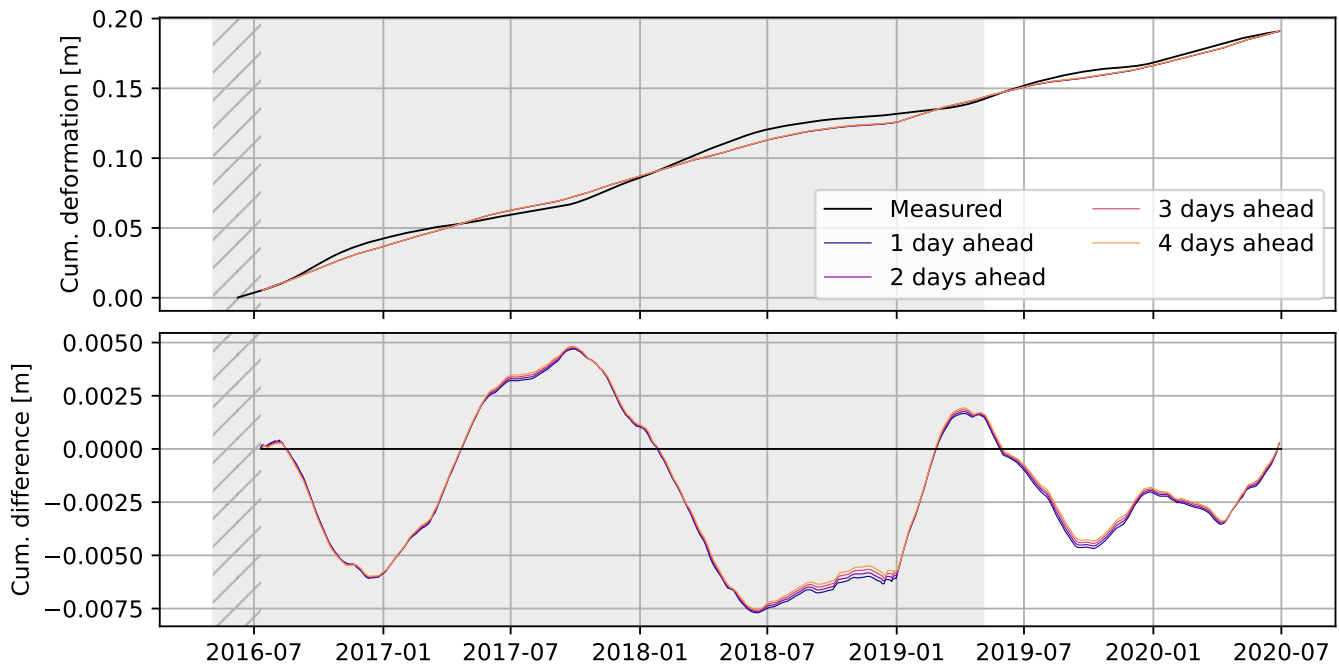


Figure 8. The cumulative deformation, as predicted by the consecutive, individual model runs closely matches the observed deformation over the full four years of deformation measurements. The difference is calculated as ‘modelled - observed’ ($\hat{y} - y$) cumulative deformation. The training period of the model is marked in gray, hatched are the warm-up periods of the moving average filter and memory of the model.

ERA5 (V7); and evaporation from GLEAM (V8), where the numbers refer to Table 1. The minimal mean squared error on validation was achieved when the model was trained over period 3 (Figure 6, 2016-05-04–2019-05-04), the mean squared error of this model run was $1.03 \frac{\text{cm}^2}{\text{year}^2}$, below the average of $3.15 \frac{\text{cm}^2}{\text{year}^2}$ ($\sigma \approx 1.3 \frac{\text{cm}^2}{\text{year}^2}$, from 1718 samples) for this model configuration.

The full nowcast is shown in Figure 7, including the training period shaded in gray. Although, based on visual inspection, reasonable results are achieved in summer and autumn, the nowcasting model is unable to predict the deformation rate in winter and spring in the training period. Especially surprising is the jump in the winter of 2018/2019, where a strong acceleration is predicted which does not occur until early summer. The validation period, from 2019-05 onwards, shows little variation. The deceleration in the summer and autumn of 2019 is overestimated and shifted, likewise the acceleration in the December 2019 is predicted correctly, but too early. Overall the predictions show long-term stability (Figure 8) as enforced by the choice of the mean squared error as loss function.

The modelling results are overall unsatisfactory: the acceleration and deceleration are typically not predicted timely, or not at all. This is surprising in the light of the success reported by others (Table C1). Although we designed our model to match our understanding of the interplay of hydro-meteorological conditions and deformation, the physics behind slope processes at the

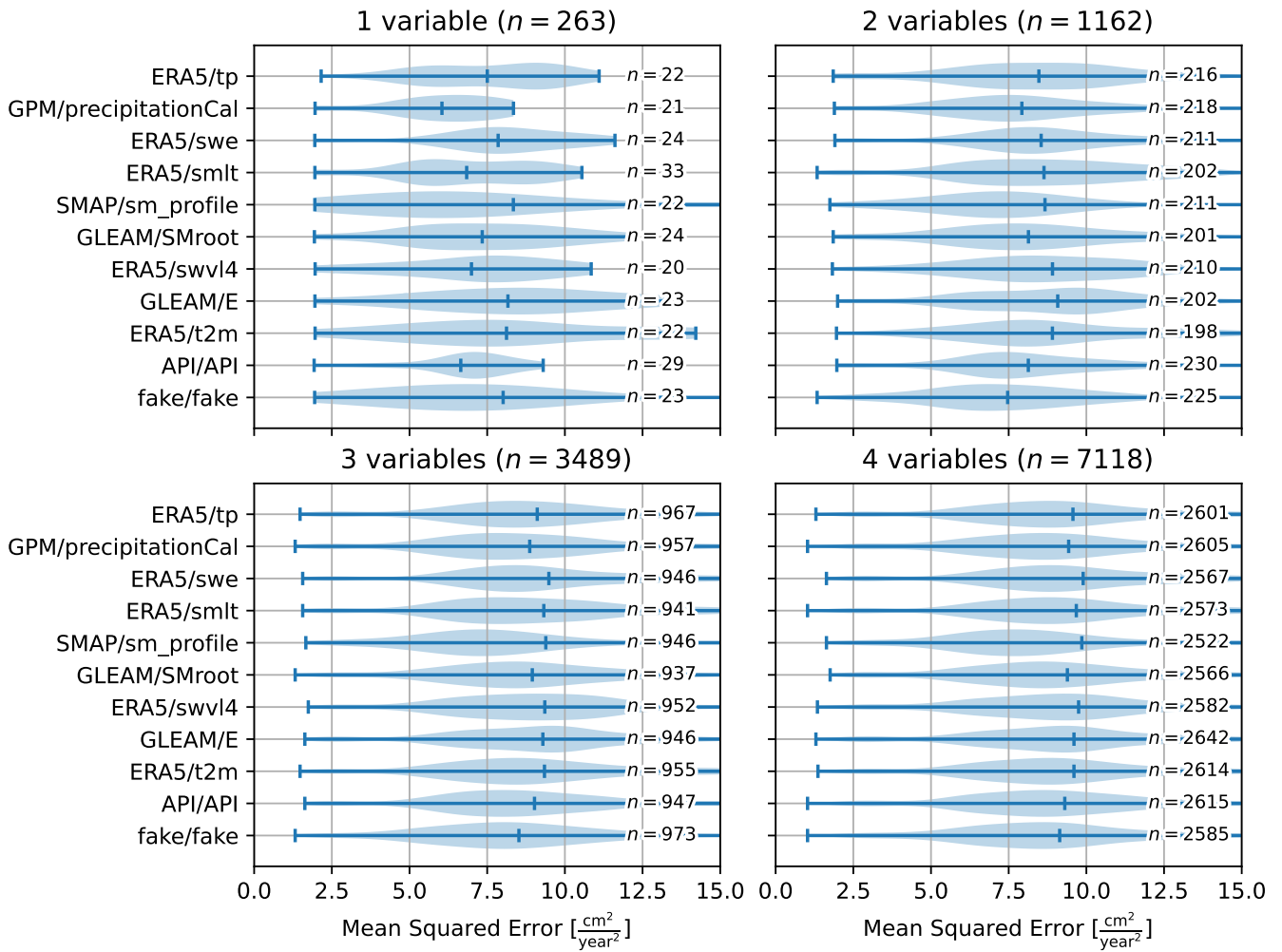


Figure 9. Violin plots of the mean squared error for model variations with one to four variables, including the variable listed. For more than four variables the relative importance of the individual variables to the model quality becomes insignificant.

Vögelsberg landslide, the model was unable to capture this relation. The deformation at Vögelsberg is driven by a complex interplay of hydro-meteorological conditions, unlike most of the examples in Table C1, that often includes a strong, stable driver, such as a reservoir. This lack of such a single, strong, driver complicates the working of our data-driven model.

310 5.1 Contribution of individual variables

Due to the complexity of the operations applied to the input signal in the LSTM layer, it is not straightforward to analyze the contribution of the individual components to the final model outcome. As all model variations were tested (§4.4), it is possible to analyze the influence of the presence of a variable by comparing the quality of the model variations. For this analysis only

model iterations with a training period (Figure 6) that left at least one year left for validation were used. Furthermore, all model
315 variations were run multiple times to assess the robustness of the outcome to the random initialisation.

Figure 9 shows the results of this analysis, and illustrates the mean squared error over the validation period for all models including each variable. For each variable the minimum and average mean squared error for the validation period are shown, while the maximum mean squared error is often out of range. The thickness of the line indicates the density of results for that mean squared error, where thicker lines at lower mean squared error indicate a concentration of models with high quality of fit.

320 Models based only on *SMAP/sm_profile* (V5) score the poorest (highest mean squared error) on average, but with the widest distribution, including many solutions with a low mean squared error. The difference in performance between the variables vanishes as more variables are introduced into the model, however, the models including the SMAP soil moisture (V5) time series show a consistently larger range in performance, including models with a low mean squared error. Remarkable is the approximately equal performance between *API/API* (V10) and *fake/fake* (V11), where the latter contains no information
325 on the hydro-meteorological processes and is only marginally outperformed by the Antecedent Precipitation Index (API, V10). For models with more than four variables, there is no significant difference in model quality for any of the variables.

6 Discussion

We believe the unsatisfactory performance of the model has three root causes: i) the inability of the model to capture the complex dynamics of the system; ii) the limited quantity of training data available to this type of problem; and iii) the limited, noisy
330 representation of the slope dynamics in the available remote sensing data. Most natural deep-seated landslides are characterized by a complex interplay of causal (antecedent) and triggering conditions: this is also true for the Vögelsberg landslide. However, we believe that it is exactly these challenges that we should aim to tackle with a machine learning model approach.

6.1 Model configuration

The possibilities for data-driven modelling are infinite: our model is only a single realisation of the possible combinations of
335 variables and operations. This raises three questions regarding the model selection: i) how to match model and process; ii) how to validate and quantify the quality the nowcast; and iii) how to tune the model implementation.

The major challenge for the model of a deep-seated landslide is the discrepancy between the sub-daily variations of the input (especially precipitation and snowmelt), and a delayed, daily output (accelerated deformation). Therefore, non time-aware models show erratic behaviour, as the consequence of sudden changes to conditions such as snow cover and as well as (extreme)
340 precipitation, that, in reality, do not translate into immediate acceleration. Traditionally, the addition of groundwater physics, smoothing the hydro-meteorological signal, circumvents these peaks. However, the addition of groundwater physics requires knowledge of the geohydrology of the specific slope.

An LSTM-node resembles a bucket model, and was chosen such to capture the delay between precipitation and deformation, by modelling the build-up of water in the model. Our results showed that our model was unable to fully capture these hydro-

Table 2. List of reference models tested for comparison to `lstm1-32`. Their performance is shown in Figure 10. To calculate the number of model parameters: n the length of the time series provided to the model, k the number of input variables, m the number of memory cells, and h the number of hidden nodes. A single hidden layer is assumed. The number of parameters includes the final, output layer of four nodes for each of the two deformation time series.

| Model | Hidden layer | Activation | History | Parameters |
|-------------------------|-----------------------|------------|---------|------------------------------------|
| <code>lstm1-32</code> | LSTM (1 memory cell) | tanh | 32 days | $4(k + m + 1)h + 2(4 \cdot m + 4)$ |
| <code>lstm3-32</code> | LSTM (3 memory cells) | tanh | 32 days | " " |
| <code>rnn1-32</code> | RNN (1 memory cell) | tanh | 32 days | $h(k + m + 1) + 2(4 \cdot m + 4)$ |
| <code>rnn3-32</code> | RNN (3 memory cells) | tanh | 32 days | " " |
| <code>rnn3lin-32</code> | RNN (1 memory cell) | none | 32 days | " " |
| <code>da-32</code> | 8 cells | none | 32 days | $h \cdot k + 2(4 \cdot h + 4)$ |
| Lin. Least Sq. | none | none | | $2(n \cdot k \cdot 4 + 4)$ |

345 meteorological dynamics. For reference five alternative models were implemented (Table 2), that were designed to better address the diversity of the slope, and/or lower the number of parameters required by the model to prevent over-fitting.

The `lstm3-32` model contains two additional memory cells (buckets) in the LSTM-node, compared to the `lstm1-32` model previously used. The concept is that the memory cells may represent different systems or layers in the subsurface, potentially interacting with each other. For each subsequent time step, all states are included in the calculation of the new states, and
350 could therefore also model interactions between layers in hydrology, such as the transfer of between layers. The `rnn1-32` and `rnn3-32` models based on a traditional Recurrent Neural Network are similar to their LSTM counterparts, with one and three memory cells respectively. However, unlike an LSTM-node, they are unable to ‘forget’ their state on command, and are more susceptible to unstable behaviour. The `rnn1lin-32` did not incorporate an activation function and is comparable to a
355 equivalent LSTM based models.

The `da-32` model resembles a linear least squares model. Variables are first summarised as their average over their 32-day history, and included in eight nodes without bias in the hidden layer of the network. The final predictions are a linear combination of the node values. In a ‘traditional’ linear least squares solution, a direct combination of all input variables, the number of parameters will often outnumber the number of observations available, and was therefore not tested.

360 The performance of each model is shown for comparison in Figure 10, as function of the parameters required. Model performance is typically optimal for models with only a single parameter, and is comparable between the models. Like the original model (`lstm1-32`), each model was re-run multiple times with a random initialisation of the seasonal noise (V11) and model parameters, to verify the consistency of the output. Most alternative models do not outperform the average deformation rate as predictor for the future deformation rate, as shown in Figure 10.

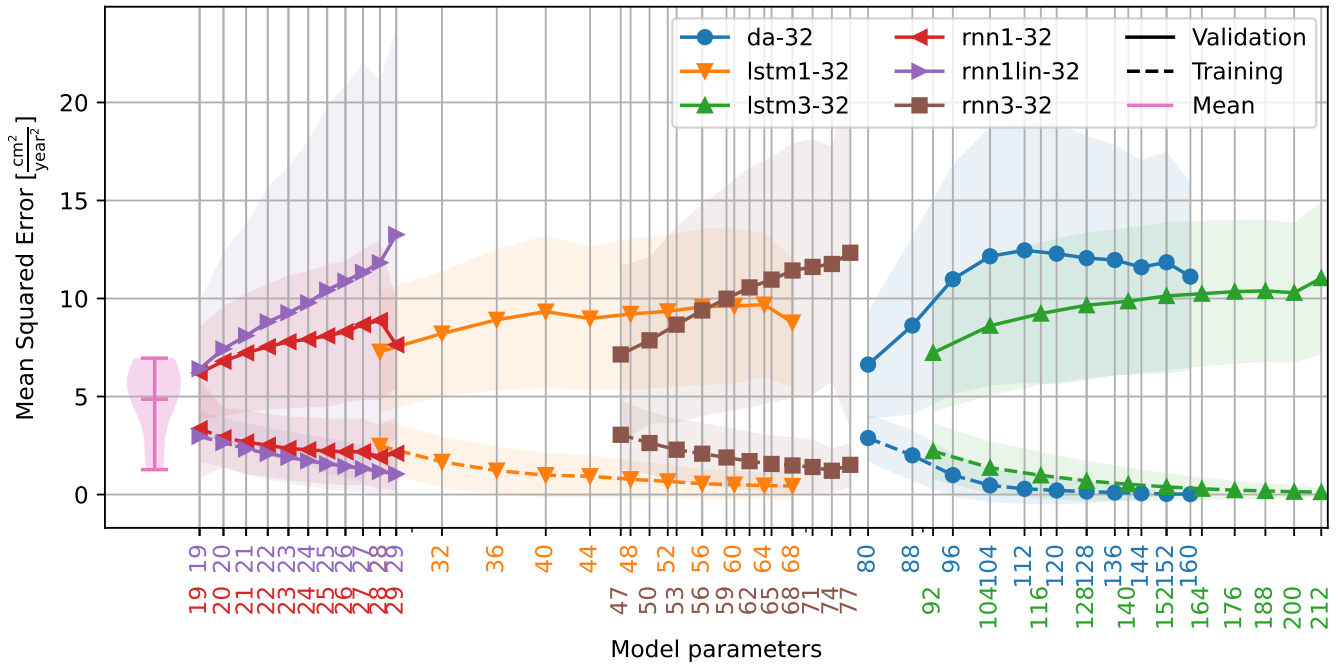


Figure 10. Relationship between the number of model parameters and the quality (mean squared error) of training and validation as extracted from the 147 984 model runs. The number of parameters is related to the number of input variables. For LSTM based networks, for example, there are four parameters per input variable per LSTM memory cell required. Note the logarithmic scale on the x-axis. On the left, the mean squared error is shown would the mean deformation rate be used as a nowcast, based on all nine training periods (Figure 6).

365 6.1.1 Performance metric

For early warning systems, prediction of the onset of acceleration (Figure 11) is more important than the deformation quantity. However, false alarms, triggered by insignificant accelerations, may undermine confidence in the early warning system. At this stage of development, we would rely on professional interpretation by an expert to limit the number of false alarms. However, the system should warn the expert for potentially bad predictions, for example due to previously not encountered conditions.

370 The timing of the nowcast should allow for further analysis of the prediction without jeopardising precautionary measures for accelerated deformation.

This leads to five desired properties for the nowcasting system: the system should i) predict onset of acceleration; as well as ii) the maximum deformation velocity; iii) four or more days ahead that deformation will begin; iv) predict when the slope is 'stable' again; and v) quantify the certainty in the prediction. Unlike most estimation problems, the timing and not only the

375 quantity of the predicted deformation is important to the user. An acceleration phase predicted too early or slightly late may still trigger the desired alertness, and still serve a purpose, even though the predicted amplitude on that day is wrong.

A ‘standard’ error metric, e.g. the mean squared error, is sensitive to the mean as local optimum, but is unbiased and therefore stable in the long term. As an alternative such error metric could be evaluated at ‘peaks & valleys’, the peaks of the deformation rate, only, emphasizing extremes and disregarding their onset. With this method there are less samples, only the extremes, 380 but they are less correlated and include the amplitude of the event. Although this captures the timeliness of the extremes, it disregards timing of the onset and pattern of the acceleration phase. Moreover, this approach requires information on the peaks and valleys, and that those are correctly identified beforehand.

Due to the lack of information on the extremes of the deformation, we chose to use the mean squared error as error metric. This metric ensured a long term stability, and connected stability of the deformation nowcast, as demonstrated by the cumulative 385 deformation (Figure 8). As a consequence, the system preferred ‘average’ solutions, overestimating the deformation rate in stable periods and underestimating the deformation rate in periods of accelerated deformation. For reference, the mean deformation rate was determined over each of the nine training periods (Figure 6) and used as ‘predictor’ for the remainder of the time series. This constant deformation rate ‘model’ outperforms many of the more parameter heavy models over the validation period and its mean squared error is shown on the left of Figure 10.

390 Accelerations of the Vögelsberg landslide are known to be triggered by precipitation in summer/autumn and by snowmelt in winter/spring (Pfeiffer et al., 2021). Simple models, based on a limited number of variables and/or with limited modelling freedom, may not be able to cope with both driving forces. As a consequence, their overall performance will be poor. The overall performance, however, does not reflect the performance per season or acceleration trigger. Therefore, to make such model behavior explicitly visible, seasonal differences in performance could be included in the evaluation of the model’s 395 performance for example by evaluating a model’s performance metric per season as well. Training the model per season, however, will require sufficient, dynamic training data to be available over each season, severely reducing the length of time series available.

6.1.2 Derived variables

Additional variables may be derived from the direct observations. In our model, the Antecedent Precipitation Index (API) 400 is such derived observation, and was chosen to enhance the information content of the hydro-meteorological observations to the model (i.e. provide higher predictive power to the model). This ‘feature generation’ is an important component of more traditional machine learning techniques, where the system is not expected to derive those relations autonomously. Derived, additional features were extensively used by Krkač et al. (2020, 2017), for example, who created additional features to capture the conditions on the landslide, or Miao et al. (2022) who derived ten features from only two sources (rainfall, reservoir level). 405 Drawback of the addition of large quantities of such derived variables to the system is that each additional time series requires additional model parameters to be optimized.

6.1.3 Handling unencountered conditions

Given the limited availability of deformation measurements, most of the data is required to train the model. Moreover, the variation in conditions is limited to the variation in those five years. It is therefore likely that the model will encounter conditions in operation that it had not encountered before. The continuous nature of the model proposed, and the alternatives discussed in §6.1, the output for such conditions is not bound to the previously encountered conditions.

For simple combinations of variables, i.e. of a single or a few variables, the response may be tested empirically. Note that the full 32-day history has to be included in this simulation. However, the response may not be so straightforward: a warm summer day combined with hail from a thunderstorm may trigger an unrealistic ‘path’ in the model. Therefore, for more variables, the number of potential combinations increases drastically and may no longer be feasible to simulate.

Predictions of extraordinary responses are not necessarily undesirable, an unbound acceleration, i.e. landslide collapse, prediction should be possible. However, the model would preferably warn for a potential unstable state of the nowcasting system. This could be achieved by an ensemble of models, either based on the same model, or model variations. Especially models with different time series lengths may be able to help pinpoint the source of the discrepancy.

6.1.4 Spatial distribution

Our model of Vögelsberg is based on two benchmarks, that are on two distinct sections of the slope (Figure 1) that have shown to exhibit different deformation behaviour. The southern, inhabited part of the slope exhibits constant deformation, with limited acceleration in wet periods. In contrast, the benchmark on the northern part of the slope shows strong accelerations and deceleration as a delayed response to strong precipitation (Pfeiffer et al., 2021). Although our models are unaware of this spatial relationship, it is found empirically during training as the shared LSTM-node, representing the slope processes, is weighed differently for each benchmark.

As an alternative, a location index could be specified, for example as binary indicator of the landslide section, or as continuous signals such as a distance to the centre. Instead of two or more predefined outputs from the same model, a single model may handle different benchmarks differentiated by additional input variables encoding their position within the system. However, given the shallow model design, care should be taken to design the model such that this index works as a scaled multiplier of the hydro-meteorological conditions.

6.2 Limited number of distinct events

Over the full time span of the measurements, four distinct acceleration periods can be identified (Figure 11). Especially these acceleration periods are of interest to an early warning system, as they mark the start of a period of accelerated deformation and associated hazard. Although the periods of accelerated deformation are comparable in length to the periods of continued, but reduced, deformation, the acceleration events are much shorter (Figure 11). Therefore, these periods are underrepresented in error metric during training and validation. However, training on these four periods alone leave insufficient variability to

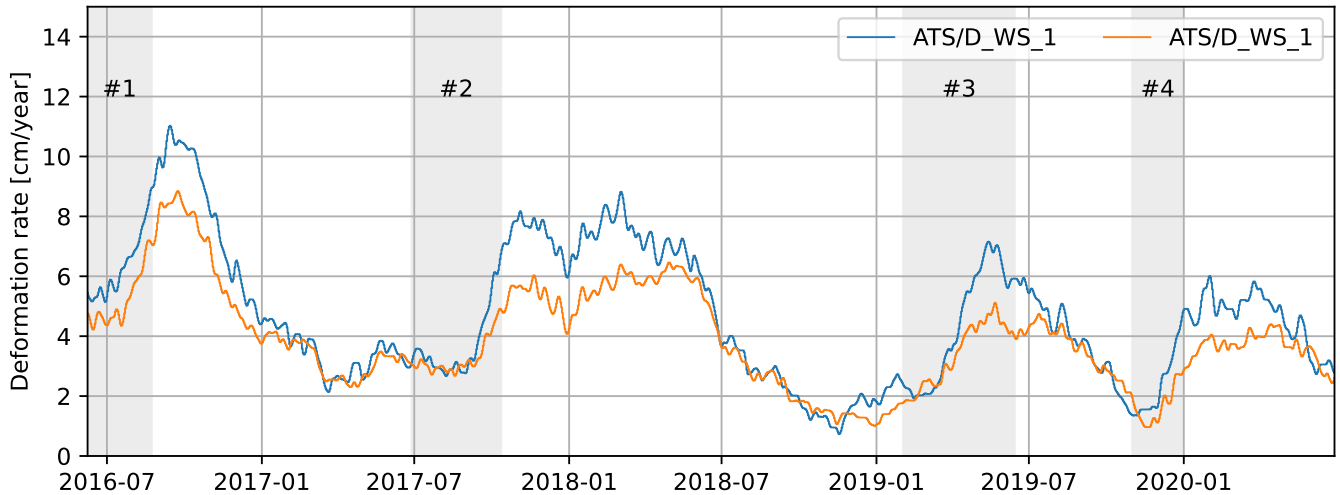


Figure 11. Three acceleration events (#1, #2 & #3) at the Vögelsberg landslide, as identified by Pfeiffer et al. (2021). The fourth acceleration period (#4) was identified in the data acquired after Pfeiffer et al. (2021).

describe the system and reliably fit the required model parameters. Furthermore, the episodic deformation behaviour poses a challenge to the prediction system since the forcing variables on the slope do not reflect such sudden changes observed in the deformation behaviour, as shown in Figure 3.

6.2.1 Length of training

Given there is more than a single degree of freedom in the model, without prior knowledge of the process, there is no predictive power in a single acceleration event. Hence, multiple events are required to properly train complex models, in the absence of constraints on the process/model. As a consequence, due to the limited variety of events in the training data, the predictive power of the nowcasting system may be reduced, due to over-fitting on the characteristics of these events only.

To test the effect of the training length on the models, the models were trained on nine of the ten training periods identified in Figure 6 that had a least a year left for validation. The mean squared error, measured on the training as well as validation period, is shown in Figure 12. The results are consistent between the models: all models show that as the training period increases, the quality over the training period decreases (dashed line, increasing mean squared error) due to the increased variability of the events therein. Likewise, the quality over the validation period increases (solid line, decreasing mean squared error), as the model generalizes better. This is also reflected in the lower standard deviation for validation over longer training periods. Hence, a longer training period makes the system more robust against the variations encountered by the system.

To train and validate the nowcasting system, the time series was subdivided in calendar years measured from the start of the measurements. An alternative, common subdivision would be in hydrological years or water years, that are typically defined to be from October 1 to September 30 and divided by the precipitation minimum (Lins, 2012). This subdivision is typically

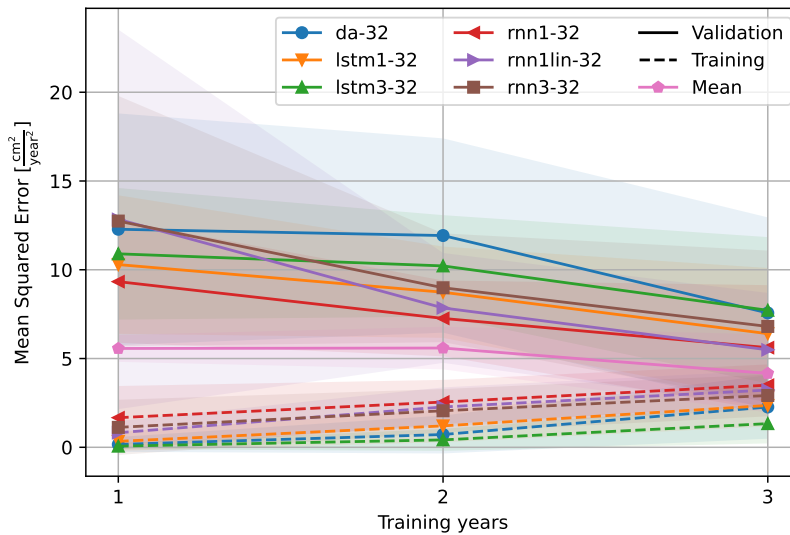


Figure 12. Length of the training region, aggregated to (approximate) years, compared to the quality of fit of the model, measured as the mean squared error. An increase in model fit is visible with the increase in training length, however, most models are outperformed by the models that use the mean deformation rate (pink) of 1, 2 or 3 years, respectively, as a the predictor.

applied to cut the data in a hydro-meteorologically quiet period of the year. However, the strong deformation events in period 1 and 2 overlap with this subdivision. Furthermore, with this subdivision, only three periods would be available, instead of four. Moreover, Parajka et al. (2009) show that the period of minimum precipitation cannot be pinpointed to a single winter month. Therefore, the decision was made to align the training years with the measurements instead.

460 6.2.2 Noise reduction of the deformation signal

Essential to the success of the nowcast are the properties of the signal to be predicted. The effect of noise in the deformation signal on the modelling is twofold: first, random perturbation complicates the training by masking the best solution, and, second, leads to an underestimation of the final quality of the model during validation. Hence, the noise in the deformation signal defines the upper limit for the quality of the deformation estimate. Up-slope deformation, present in the raw deformation time series, was considered to be unrealistic and therefore noise by definition. Under the assumption that the noise is unbiased, 465 the noise will be reduced in averaged samples. Therefore, a moving average filter was applied to the deformation time series with increasing length until no negative deformation remained.

The model was developed with the requirements for an operational system in mind, restricting the system to only use historic observations at any point in the process. Inclusion of future samples would require the system to react to future conditions that 470 have not (yet) been observed on the slope: any filtering, such as smoothing, should not drag future observations back in time.

Therefore, the moving average filter cannot be centered, and averaging is applied to the preceding 31-days, rather than ± 15 days around the current time step as would be possible in re-analysis.

The variation in the deformation signal at Vögelsberg is relatively small, in deviation from a long term trend. Due to the millimeter-scale measurement uncertainty in the deformation measurements, the deformation signal is dominated by noise on
475 the short time scale of days to weeks, the relevance of a deformation prediction on a daily basis is doubtful. Furthermore, due to the inertia of the landslide body, as well as smoothing of the deformation measurements, accelerations and decelerations are spread over adjacent days (Figure 6) and the amplitude of the acceleration is lost. For a successful, daily application, a clear separation between events and noise is required (higher signal to noise ratio), either due to a faster process, or due to reduced noise in the deformation observations.

480 6.3 Input variables

The variable selection in Table 1 was compiled based on our knowledge of the physics behind the landslide process, as well as the availability and continuity of the data. With the ambition for a future, regional implementation in mind, the variables preferably come from satellite remote sensing observations rather than local, field sensors. However, we did not succeed in a fully remote sensing driven operation, due to the limited availability of such operational products. Especially deformation
485 observations from space ('InSAR') were found to be promising but we were unable to replace our local deformation time series with the noisier satellite deformation data.

6.3.1 Availability of variables

The model was designed under the assumption that data from all sources is continuous and readily available to the system. ~~Traditionally, local weather and groundwater monitoring stations provide timely, local, high quality observations. However, such monitoring stations are not available everywhere.~~ Out of the variable selection (Table 1) only GPM (V2) and SMAP (V5) satisfy this condition of timely availability and provide operational data products, that could be integrated in a nowcasting solution. Traditionally, local weather and groundwater monitoring stations provide timely, local, high quality observations. However, such monitoring stations are not available everywhere. Therefore, we choose not to compare the local observations from on and around the Vögelsberg with the satellite products.

495 For a successful integration of satellites observations in an operational nowcasting system, a high, sub-weekly, update frequency is required. However, most remote sensing products were available at a delay of days to weeks, still too late for integration in a nowcasting system. As a consequence, the variable selection in Table 1 contains variables that are only available in yearly iterations (e.g. GLEAM).

Satellite radar interferometry (InSAR) is a proven method for landslide deformation monitoring (Colesanti and Wasowski,
500 2006; Hilley et al., 2004). However, especially mountainous environments create a complex interplay of local atmospheric effects and topography (Hanssen, 2001). A feasibility study showed that the slope orientation and topography would allow for the application of Sentinel-1 satellite radar deformation measurements at Vögelsberg (van Natijne et al., 2022). Further

processing of Sentinel-1 data demonstrated the presence of persistent scatterers on and around the houses at the slope, the objects of primary interest. However, the use of satellite based InSAR as source of the deformation measurements was not
505 feasible, due to the low temporal resolution, as well as the noise in the deformation signal (Zieher et al., 2021).

6.3.2 Data continuity

Temporal continuity of input data is required to provide the model with consistent samples of the slope conditions. Short periods of missing data, e.g. days, may be forward filled, but will reduce the data quality for the full integration length (i.e. 32 days). Observations received late may still be updated in later iterations, to mitigate this effect. However, what to do with
510 missing data: a single day or a whole season, or the termination of a data source, for example due to satellite failure? As a fallback one could model and train systems with different variable combinations in advance, and nowcast based on the best model available for the variable combination available in the 32 days prior.

The LSTM-nodes may be implemented in a stateful fashion, where the state of the hidden nodes is retained after each prediction. Such implementation is more computationally efficient, as each subsequent nowcast will require only a single pass over
515 the most recent data. In such implementation, however, discontinuous or erroneous variables may have a lasting effect on the model memory. Therefore, the system was based on continuous re-initialisation with a 32-day observation history instead. The computational drawback is limited, given the small scale of the model, and is acceptable in the light of the greater operational flexibility.

6.3.3 Variables not related to the hydro-meteorological cycle

Indirect observations of the hydro-meteorological cycle may still prove valuable to the nowcasting system. The temperature, for
520 example, may serve as a proxy indicator for evaporation. Temperature is related to the seasons in most climates, and therefore there will be a correlation with the season (day-of-year) as well. However, extra care should be taken including variables that describe the typical/average condition, such as the season. Such variables do not capture the current dynamics of the system and may only describe average conditions, and constrain the system in extraordinary circumstances. The Vögelsberg landslide
525 is known to be sensitive due to changes in the ground water level, irrespective of the season.

6.3.4 Input variable selection

The success of a data-driven model lies in the (expert) selection of the input data. Unrelated variables make the system prone to spurious correlations, especially with limited training data compared to the degrees of freedom in the model or if the method is unable to discard or otherwise ignore sources with low information content. Furthermore, unrelated input variables, or even
530 just noise, should not yield sensible results: “garbage in, garbage out”.

The effect of noise in the conditions was tested by the inclusion of a Brownian motion signal (see §4.4), that does not have a relation to the system, except for basic properties (i.e. mean, standard deviation, autocorrelation period) similar to the input variables. Any model run including this signal should not outperform an otherwise comparable model without this variable.

However, many of the models did, especially when many (≥ 5) variables were included, where it helped to create unique
535 variable combinations and allowed the model to over-fit.

Parameters on geology and topography were left out of the selection, and assumed static. However, neither were land cover
changes included. In the case of Vögelsberg, it was known that little changes were to be expected over the time frame of the
measurements available. An alternative to the inclusion of such variables is to frequently re-train the model on a recent section
of the time series only to adapt to changes. However, although the system will adapt to changing dynamics, re-learning will
540 mask the drivers behind long term effects, and/or adapt too swiftly, for example to seasonal differences, reducing the overall
model quality. Land cover changes will not be uniform across slopes, as well as act on different time scales (e.g. neglected
pasture fields versus forest fires), and may not be trivial to capture by remote sensing. Moreover, especially in regional studies,
the land cover and land cover change may not be comparable between slopes.

To limit the number of variables, only the observation or modelling result closest to the Vögelsberg landslide was used from
545 regional products. However, as Pfeiffer et al. (2021) found, precipitation and snow-melt higher up in the catchment is relevant
for the system (Figure 1). Based on the typically low ($\simeq 10$ km) spatial resolution of the variables (Table 1) it is justified to
consider a single observation only. When higher resolution observations are added, this should be reconsidered, and additional
points may be added as extra variables.

6.4 Outlook

550 Our results show that deformation nowcasting is an open challenge. Although well monitored, the Vögelsberg landslide is a
complex system, and therefore not a straightforward test case. Our results are inconclusive whether our method could work
on other deep-seated landslides. More direct dynamics, and/or stronger and more frequent acceleration periods would help
constrain the system. The inclusion of field data, such as groundwater level (Krkač et al., 2020), might be another approach to
bypass modelling of the most volatile hydrological processes. The ideal slope to further develop a machine learning based now-
555 casting method has the following characteristics: i) a dynamic deformation behaviour; ii) is controlled by hydro-meteorological
conditions, with limited delay; and iii) has field monitoring data for reference and training.

For short time series machine learning methods are known to be outperformed by basic statistical methods (Makridakis et al.,
2018). Therefore, our current challenge to nowcast deformation time series may be partially solved in the near future by the
natural extension of time series. Furthermore, continued development of the (satellite) data products by their providers may
560 enable new possibilities. Desirable improvements include timeliness of delivery of data products, as well as their precision and
spatio-temporal resolution.

Notable is the recent publication of the first version of the European Ground Motion Service data set (Crosetto et al., 2020),
a pan-European InSAR product. This data set will allow for experimental, regional, weekly nowcasting systems based on a
replay of historic observations. Regional applications will enhance training possibilities and may help overcome the hurdle

565 of limited deformation time series, as multiple slopes are monitored simultaneously. However, to ‘learn’ from the differences between slopes, and enlarge variation in training data, events have to be largely uncorrelated.

7 Conclusions

Although Vögelsberg is a well monitored landslide, the number of recorded acceleration events, within the available four years of daily deformation measurements, is limited compared to other machine learning problems. A simple, time series capable
570 model with limited parameters was required, therefore, we designed an LSTM-based machine learning algorithm to nowcast the deformation of the Vögelsberg deep-seated landslide from the conditions on the slope. The algorithm was trained on maximum three years of deformation observations and satellite observations of relevant hydro-meteorological conditions at the slope. The best model configuration and variable combination was determined by cross-validation with 147 984 model variations.

Although rooted in the landslide dynamics, even our best model was incapable of capturing the versatility of responses of the
575 Vögelsberg landslide, and convincingly predict the deformation rate at Vögelsberg four days ahead. Especially the four acceleration events were not predicted timely, although the mean squared error successfully constrained the average deformation rate of the prediction to that of the training time series. The Vögelsberg landslide showed versatile dynamics, where the full range of slope dynamics and responses to the hydro-meteorological conditions were not present in the available data. Therefore, the slope processes were too complex to model the landslide deformation from satellite surface observations, given the limited
580 observations of acceleration events. Hence, the machine learning model was incapable of ‘understanding’ the relation between conditions and deformation.

Deformation nowcasting will be a necessity for regional or even continental landslide monitoring and early warning systems. Satellite remote sensing has the potential to provide longer time series, over wide areas. This leads us to the general recommendation for the application of machine learning to reactivating, deep-seated, landslides: improve data quality, and lengthen
585 the deformation time series. The ideal landslide for further development of deformation nowcasting: is highly dynamic (many events to train on), has a limited delay between forcing conditions and deformation, is well monitored, and does not undergo catastrophic failure.

Appendix A: Data

See Figure A1.

590 Appendix B: Total Station

See Figure B1.

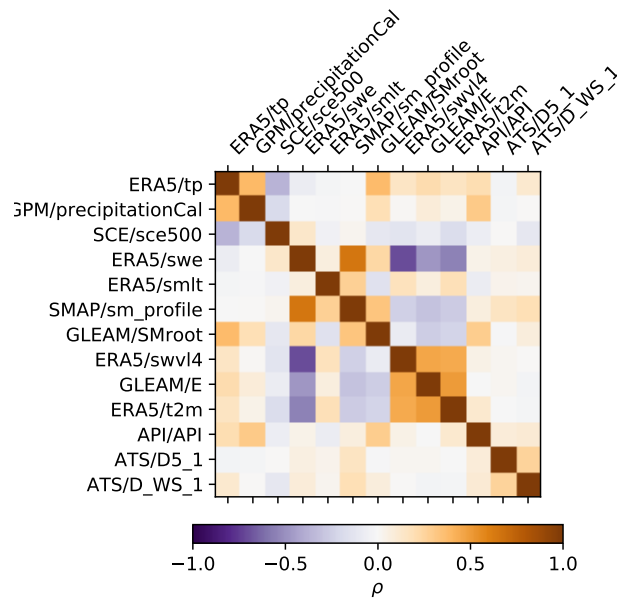


Figure A1. Correlation between variables.

Appendix C: Models

C1 State-of-the-art

See Table C1.

595 *Author contributions.* **A.L. van Natijne:** Methodology; Software; Formal analysis; Writing - Original Draft. **T.A. Bogaard:** Conceptualization; Writing - Review & Editing; Supervision. **T. Zieher:** Resources; Writing - Review & Editing. **J. Pfeiffer:** Resources; Writing - Review & Editing. **R.C. Lindenbergh:** Writing - Review & Editing; Supervision.

Competing interests. The authors declare that they have no known competing financial interests or personal relationships that could have appeared to influence the work reported in this paper.

600 *Acknowledgements.* This work was carried out under the framework of the operandum (OPEn-air laboRAtoRies for Nature baseD solUtions to Manage hydro-meteo risks) project, which is funded by European Union's Horizon 2020 Framework Programme for research and innovation under grant agreement 776848.

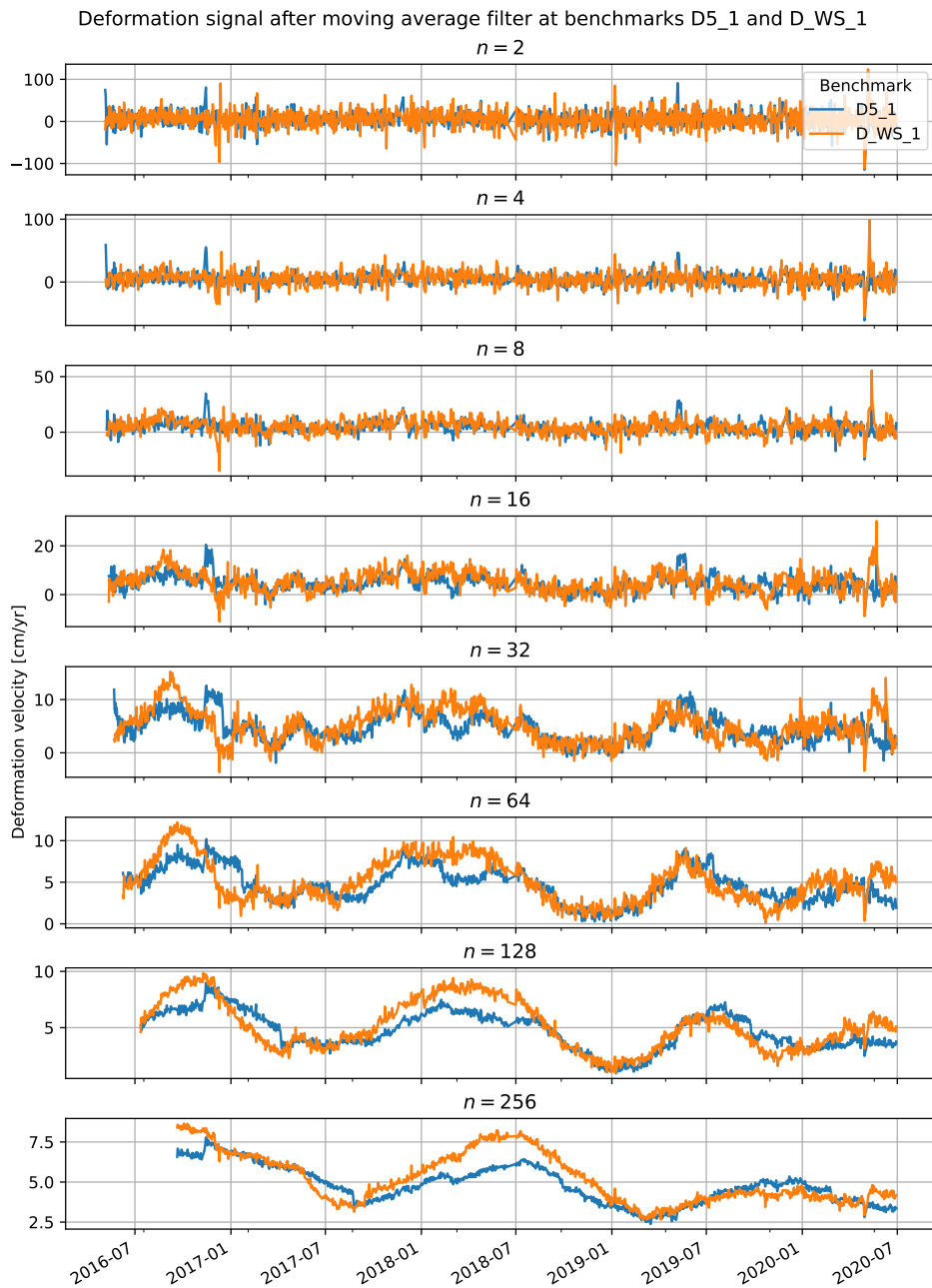


Figure B1. Smoothed deformation signal, shown for an increasing length (in days) of the moving average filter. The filter only includes historic observations, and is not 'centred', to match the properties of an operational system. The increasing time lag is visible for the subsequent filter lengths by the right shifting of the velocity peaks. For initial observations, a filter length of half the final length of the filter was accepted.

Table C1. Examples of different integration methods, linking hydro-meteorological conditions to deformation time series, and associated case studies. Most studies are at deep-seated landslides that did not undergo catastrophic collapse. Studies with and without reservoir level as observation are grouped together. Updated after van Natijne et al. (2020).

| | Case study | China | Obs. driving forces | Deform. meas. | Notes |
|--------------------------------|----------------------------|----------------|---|------------------------------|---------------|
| Zhang et al. (2021) | Fengning, | China | Rainfall, toe excavation (incl. blasting) | Total station, inclinometer, | |
| Deng et al. (2021) | Hollin Hill, | United Kingdom | Rainfall, acoustic | fiature meter | |
| Krkač et al. (2020) | Kostanjek, | Croatia | Rainfall, groundwater | Inclinometer | |
| Bosso and Marcato (2019) | Passo della Morte, | Italy | Rainfall, groundwater | GNSS | |
| Liu et al. (2021) ^a | Longnan, | China | Rainfall | Inclinometer | |
| Xie et al. (2019) | Laowuji, | China | Rainfall, toe excavation | Total station | |
| Huang et al. (2017) | Baishuihe & Bazimen, | China | Deformation | GNSS | |
| Krkač et al. (2017) | Kostanjek, | Croatia | Groundwater (change), season | GNSS | |
| Logar et al. (2017) | Ventor, | United Kingdom | Rainfall | Crackmeter | |
| Zhu et al. (2017) | Kualiangzi, | China | Rainfall | GNSS | |
| Cai et al. (2016) | Xiluodo, | China | Rainfall | Extensometers | |
| Liu et al. (2014) | Baishuihe, | China | Deformation | GNSS | |
| " " | Super-Sauze, | France | Deformation | Extensometer | |
| Chen and Zeng (2013) | Baishuihe, | China | Deformation | GNSS | |
| Corominas et al. (2005) | Vallcebre, | Spain | Groundwater | Extensometers | Physics based |
| Neaupane and Achet (2004) | Okharpauwa, | Nepal | Rainfall, groundwater | Autoextensometer | |
| Miao et al. (2022) | Baishuihe, | China | Rainfall, reservoir level | GNSS | |
| Li et al. (2021) | Baishuihe & Bazimen, | China | Rainfall, reservoir level | GNSS | |
| Liu et al. (2020) | Baishuihe, Bajijabao, | China | Rainfall, reservoir level | GNSS | |
| Li et al. (2019) | Baishuihe, | China | Rainfall, reservoir level | GNSS | |
| Wang et al. (2019) | Tanjiahe, | China | Rainfall, reservoir level | GNSS | |
| Yang et al. (2019) | Baishuihe & Bazimen, | China | Rainfall, reservoir level | GNSS | |
| Li et al. (2018) | Baishuihe, | China | Rainfall, reservoir level | GNSS | |
| Miao et al. (2018) | Baishuihe, | China | Rainfall, reservoir level | GNSS, inclinometer | |
| Ma et al. (2017) | Zhujiadan, | China | Rainfall, reservoir level | GNSS | |
| Wen et al. (2017) | Shupting, | China | Rainfall, reservoir level | GNSS | |
| Cao et al. (2016) | Bajijabao, | China | Rainfall, res. level, groundw. | GNSS | |
| Zhou et al. (2016) | Bazimen, | China | Rainfall, reservoir level | GNSS | |
| Jiang and Chen (2016) | Baishuihe & Liangshuijing, | China | Rainfall, reservoir level | GNSS | |
| Lian et al. (2015) | Baishuihe & Bazimen, | China | Rainfall, reservoir level | GNSS | |
| Ren et al. (2015) | Shupting, | China | Rainfall, reservoir level | GNSS | |
| Du et al. (2013) | Baishuihe & Bazimen, | China | Rainfall, reservoir level | GNSS, inclinometer | |

^aAnalysis, allows for prediction.

References

- Belward, A. S. and Skjøien, J. O.: Who launched what, when and why; trends in global land-cover observation capacity from civilian earth observation satellites, *ISPRS Journal of Photogrammetry and Remote Sensing*, 103, 115–128, <https://doi.org/10.1016/j.isprsjprs.2014.03.009>, 2015.
- Bengio, Y., Simard, P., and Frasconi, P.: Learning long-term dependencies with gradient descent is difficult, *IEEE Transactions on Neural Networks*, 5, 157–166, <https://doi.org/10.1109/72.279181>, 1994.
- Bogaard, T. A. and Greco, R.: Landslide hydrology: from hydrology to pore pressure, *Wiley Interdisciplinary Reviews: Water*, 3, 439–459, <https://doi.org/10.1002/wat2.1126>, 2015.
- Bossi, G. and Marcato, G.: Planning landslide countermeasure works through long term monitoring and grey box modelling, *Geosciences*, 9, 185, <https://doi.org/10.3390/geosciences9040185>, 2019.
- Cai, Z., Xu, W., Meng, Y., Shi, C., and Wang, R.: Prediction of landslide displacement based on GA-LSSVM with multiple factors, *Bulletin of Engineering Geology and the Environment*, 75, 637–646, <https://doi.org/10.1007/s10064-015-0804-z>, 2016.
- Cao, Y., Yin, K., Alexander, D. E., and Zhou, C.: Using an extreme learning machine to predict the displacement of step-like landslides in relation to controlling factors, *Landslides*, 13, 725–736, <https://doi.org/10.1007/s10346-015-0596-z>, 2016.
- Carlà, T., Intrieri, E., Di Traglia, F., Nolesini, T., Gigli, G., and Casagli, N.: Guidelines on the use of inverse velocity method as a tool for setting alarm thresholds and forecasting landslides and structure collapses, *Landslides*, 14, 517–534, <https://doi.org/10.1007/s10346-016-0731-5>, 2017.
- Cerqueira, V., Torgo, L., and Soares, C.: Machine learning vs statistical methods for time series forecasting: size matters, <https://doi.org/10.48550/ARXIV.1909.13316>, 2019.
- Chen, H. and Zeng, Z.: Deformation prediction of landslide based on improved back-propagation neural network, *Cognitive Computation*, 5, 56–62, <https://doi.org/10.1007/s12559-012-9148-1>, 2013.
- Colesanti, C. and Wasowski, J.: Investigating landslides with space-borne Synthetic Aperture Radar (SAR) interferometry, *Engineering Geology*, 88, 173–199, <https://doi.org/10.1016/j.enggeo.2006.09.013>, 2006.
- Connor, J., Martin, R., and Atlas, L.: Recurrent neural networks and robust time series prediction, *IEEE Transactions on Neural Networks*, 5, 240–254, <https://doi.org/10.1109/72.279188>, 1994.
- Copernicus Climate Change Service: ERA5-Land hourly data from 2001 to present, <https://doi.org/10.24381/CDS.E2161BAC>, dataset, 2019.
- Corominas, J., Moya, J., Ledesma, A., Lloret, A., and Gili, J. A.: Prediction of ground displacements and velocities from groundwater level changes at the Vallcebre landslide (Eastern Pyrenees, Spain), *Landslides*, 2, 83–96, <https://doi.org/10.1007/s10346-005-0049-1>, 2005.
- Crosetto, M., Solari, L., Mróz, M., Balasis-Levinsen, J., Casagli, N., Frei, M., Oyen, A., Moldestad, D. A., Bateson, L., Guerrieri, L., Comerci, V., and Andersen, H. S.: The evolution of wide-area DInSAR: from regional and national services to the European ground motion service, *Remote Sensing*, 12, 2043, <https://doi.org/10.3390/rs12122043>, 2020.
- Deng, L., Smith, A., Dixon, N., and Yuan, H.: Machine learning prediction of landslide deformation behaviour using acoustic emission and rainfall measurements, *Engineering Geology*, 293, 106–115, <https://doi.org/10.1016/j.enggeo.2021.106315>, 2021.
- Du, J., Yin, K., and Lacasse, S.: Displacement prediction in colluvial landslides, Three Gorges Reservoir, China, *Landslides*, 10, 203–218, <https://doi.org/10.1007/s10346-012-0326-8>, 2013.
- Entekhabi, D., Njoku, E. G., O’Neill, P. E., Kellogg, K. H., Crow, W. T., Edelstein, W. N., Entin, J. K., Goodman, S. D., Jackson, T. J., Johnson, J., Kimball, J., Piepmeier, J. R., Koster, R. D., Martin, N., McDonald, K. C., Moghaddam, M., Moran, S., Reichle, R., Shi, J. C.,

- 640 Spencer, M. W., Thurman, S. W., Tsang, L., and Van Zyl, J.: The Soil Moisture Active Passive (SMAP) mission, *Proceedings of the IEEE*, 98, 704–716, <https://doi.org/10.1109/JPROC.2010.2043918>, 2010.
- Fell, R., Corominas, J., Bonnard, C., Cascini, L., Leroi, E., and Savage, W. Z.: Guidelines for landslide susceptibility, hazard and risk zoning for land-use planning, *Engineering Geology*, 102, 99–111, <https://doi.org/10.1016/j.enggeo.2008.03.014>, 2008.
- Gholamy, A., Kreinovich, V., and Kosheleva, O.: Why 70/30 or 80/20 relation between training and testing sets: a pedagogical explanation, Departmental Technical Reports (CS), https://scholarworks.utep.edu/cs_techrep/1209, 2018.
- 645 Guzzetti, F., Carrara, A., Cardinali, M., and Reichenbach, P.: Landslide hazard evaluation: a review of current techniques and their application in a multi-scale study, Central Italy, *Geomorphology*, 31, 181–216, 1999.
- Guzzetti, F., Gariano, S. L., Peruccacci, S., Brunetti, M. T., Marchesini, I., Rossi, M., and Melillo, M.: Geographical landslide early warning systems, *Earth-Science Reviews*, 200, 102973, <https://doi.org/10.1016/j.earscirev.2019.102973>, 2020.
- 650 Hanssen, R. F.: Radar interferometry: data interpretation and error analysis, vol. 2 of *Remote Sensing and Digital Image Processing*, Springer Netherlands, Dordrecht, <https://doi.org/10.1007/0-306-47633-9>, 2001.
- Hartke, S. H., Wright, D. B., Kirschbaum, D. B., Stanley, T. A., and Li, Z.: Incorporation of satellite precipitation uncertainty in a landslide hazard nowcasting system, *Journal of Hydrometeorology*, 21, 1741–1759, <https://doi.org/10.1175/JHM-D-19-0295.1>, 2020.
- Heggen, R. J.: Normalized antecedent precipitation index, *Journal of Hydrologic Engineering*, 6, 377–381, [https://doi.org/10.1061/\(ASCE\)1084-0699\(2001\)6:5\(377\)](https://doi.org/10.1061/(ASCE)1084-0699(2001)6:5(377)), 2001.
- 655 Herrera, G., Mateos, R. M., García-Davalillo, J. C., Grandjean, G., Poyiadji, E., Maftei, R., Filipciuc, T.-C., Jemec Auflič, M., Jež, J., Podolszki, L., Trigila, A., Iadanza, C., Raetzo, H., Kociu, A., Przyłucka, M., Kułak, M., Sheehy, M., Pellicer, X. M., McKeown, C., Ryan, G., Kopačková, V., Frei, M., Kuhn, D., Hermanns, R. L., Koulermou, N., Smith, C. A., Engdahl, M., Buxó, P., Gonzalez, M., Dashwood, C., Reeves, H., Cigna, F., Liščák, P., Paudiš, P., Mikulénas, V., Demir, V., Raha, M., Quental, L., Sandić, C., Fusi, B., and Jensen, O. A.: Landslide databases in the geological surveys of Europe, *Landslides*, 15, 359–379, <https://doi.org/10.1007/s10346-017-0902-z>, 2018.
- 660 Hill, T., Marquez, L., O’Connor, M., and Remus, W.: Artificial neural network models for forecasting and decision making, *International Journal of Forecasting*, 10, 5–15, [https://doi.org/10.1016/0169-2070\(94\)90045-0](https://doi.org/10.1016/0169-2070(94)90045-0), 1994.
- Hilley, G. E., Bürgmann, R., Ferretti, A., Novali, F., and Rocca, F.: Dynamics of slow-moving landslides from permanent scatterer analysis, *Science*, 304, 1952–1955, <https://doi.org/10.1126/science.1098821>, 2004.
- 665 Hochreiter, S.: The vanishing gradient problem during learning recurrent neural nets and problem solutions, *International Journal of Uncertainty, Fuzziness and Knowledge-Based Systems*, 06, 107–116, <https://doi.org/10.1142/S0218488598000094>, 1998.
- Hochreiter, S. and Schmidhuber, J.: Long short-term memory, *Neural Computation*, 9, 1735–1780, <https://doi.org/10.1162/neco.1997.9.8.1735>, 1997.
- Hornik, K., Stinchcombe, M., and White, H.: Multilayer feedforward networks are universal approximators, *Neural Networks*, 2, 359–366, [https://doi.org/10.1016/0893-6080\(89\)90020-8](https://doi.org/10.1016/0893-6080(89)90020-8), 1989.
- 670 Huang, F., Huang, J., Jiang, S., and Zhou, C.: Landslide displacement prediction based on multivariate chaotic model and extreme learning machine, *Engineering Geology*, 218, 173–186, <https://doi.org/10.1016/j.enggeo.2017.01.016>, 2017.
- Huffman, G., Stocker, E., Bolvin, D., Nelkin, E., and Jackson, T.: GPM IMERG final precipitation L3 Half Hourly 0.1 degree x 0.1 degree V05, https://doi.org/10.5067/GPM/IMERG/3B-HH/06_dataset, 2019.
- 675 Intrieri, E., Raspini, F., Fumagalli, A., Lu, P., Del Conte, S., Farina, P., Allievi, J., Ferretti, A., and Casagli, N.: The Maoxian landslide as seen from space: detecting precursors of failure with Sentinel-1 data, *Landslides*, 15, 123–133, <https://doi.org/10.1007/s10346-017-0915-7>, 2018.

- Jain, A., Jianchang Mao, and Mohiuddin, K.: Artificial neural networks: a tutorial, *Computer*, 29, 31–44, <https://doi.org/10.1109/2.485891>, 1996.
- 680 Jiang, P. and Chen, J.: Displacement prediction of landslide based on generalized regression neural networks with k-fold cross-validation, *Neurocomputing*, 198, 40–47, <https://doi.org/10.1016/j.neucom.2015.08.118>, 2016.
- Kingma, D. P. and Ba, J.: Adam: a method for stochastic optimization, arXiv, San Diego, United States of America, <https://doi.org/https://doi.org/10.48550/arXiv.1412.6980>, 2017.
- Kirschbaum, D. and Stanley, T.: Satellite-based assessment of rainfall-triggered landslide hazard for situational awareness, *Earth's Future*, 6, 685 505–523, <https://doi.org/10.1002/2017EF000715>, 2018.
- Kohler, M. A. and Linsley, R. K.: Predicting the runoff from storm rainfall, vol. 30, US Department of Commerce, Weather Bureau, 1951.
- Krkač, M., Špoljarić, D., Bernat, S., and Arbanas, S. M.: Method for prediction of landslide movements based on random forests, *Landslides*, 14, 947–960, <https://doi.org/10.1007/s10346-016-0761-z>, 2017.
- Krkač, M., Bernat Gazibara, S., Arbanas, Z., Sečanj, M., and Mihalić Arbanas, S.: A comparative study of random forests and multiple linear 690 regression in the prediction of landslide velocity, *Landslides*, 17, 2515–2531, <https://doi.org/10.1007/s10346-020-01476-6>, 2020.
- Li, C., Criss, R. E., Fu, Z., Long, J., and Tan, Q.: Evolution characteristics and displacement forecasting model of landslides with stair-step sliding surface along the Xiangxi River, three Gorges Reservoir region, China, *Engineering Geology*, 283, 105961, <https://doi.org/10.1016/j.enggeo.2020.105961>, 2021.
- Li, H., Xu, Q., He, Y., and Deng, J.: Prediction of landslide displacement with an ensemble-based extreme learning machine and copula 695 models, *Landslides*, 15, 2047–2059, <https://doi.org/10.1007/s10346-018-1020-2>, 2018.
- Li, H., Xu, Q., He, Y., Fan, X., and Li, S.: Modeling and predicting reservoir landslide displacement with deep belief network and EWMA control charts: a case study in Three Gorges Reservoir, *Landslides*, <https://doi.org/10.1007/s10346-019-01312-6>, 2019.
- Lian, C., Zeng, Z., Yao, W., and Tang, H.: Multiple neural networks switched prediction for landslide displacement, *Engineering Geology*, 186, 91–99, <https://doi.org/10.1016/j.enggeo.2014.11.014>, 2015.
- 700 Lins, H. F.: USGS hydro-climatic data network 2009 (HCDN-2009), Fact Sheet 2012-3047, USGS, <https://pubs.usgs.gov/fs/2012/3047/pdf/fs2012-3047.pdf>, 2012.
- Liu, Y., Qiu, H., Yang, D., Liu, Z., Ma, S., Pei, Y., Zhang, J., and Tang, B.: Deformation responses of landslides to seasonal rainfall based on InSAR and wavelet analysis, *Landslides*, <https://doi.org/10.1007/s10346-021-01785-4>, 2021.
- Liu, Z., Shao, J., Xu, W., Chen, H., and Shi, C.: Comparison on landslide nonlinear displacement analysis and prediction with computational 705 intelligence approaches, *Landslides*, 11, 889–896, <https://doi.org/10.1007/s10346-013-0443-z>, 2014.
- Liu, Z.-q., Guo, D., Lacasse, S., Li, J.-h., Yang, B.-b., and Choi, J.-c.: Algorithms for intelligent prediction of landslide displacements, *Journal of Zhejiang University-Science A*, 21, 412–429, <https://doi.org/10.1631/jzus.A2000005>, 2020.
- Logar, J., Turk, G., Marsden, P., and Ambrožič, T.: Prediction of rainfall induced landslide movements by artificial neural networks, *Natural Hazards and Earth System Sciences Discussions*, pp. 1–18, <https://doi.org/10.5194/nhess-2017-253>, 2017.
- 710 Ma, J., Tang, H., Liu, X., Hu, X., Sun, M., and Song, Y.: Establishment of a deformation forecasting model for a step-like landslide based on decision tree C5.0 and two-step cluster algorithms: a case study in the Three Gorges Reservoir area, China, *Landslides*, 14, 1275–1281, <https://doi.org/10.1007/s10346-017-0804-0>, 2017.
- Makridakis, S., Spiliotis, E., and Assimakopoulos, V.: Statistical and machine learning forecasting methods: concerns and ways forward, *PLOS ONE*, 13, e0194889, <https://doi.org/10.1371/journal.pone.0194889>, 2018.

- 715 Mansour, M. F., Morgenstern, N. R., and Martin, C. D.: Expected damage from displacement of slow-moving slides, *Landslides*, 8, 117–131, <https://doi.org/10.1007/s10346-010-0227-7>, 2011.
- Martens, B., Miralles, D. G., Lievens, H., van der Schalie, R., de Jeu, R. A. M., Fernández-Prieto, D., Beck, H. E., Dorigo, W. A., and Verhoest, N. E. C.: GLEAM v3: satellite-based land evaporation and root-zone soil moisture, *Geoscientific Model Development*, 10, 1903–1925, <https://doi.org/10.5194/gmd-10-1903-2017>, 2017.
- 720 Miao, F., Wu, Y., Xie, Y., and Li, Y.: Prediction of landslide displacement with step-like behavior based on multialgorithm optimization and a support vector regression model, *Landslides*, 15, 475–488, <https://doi.org/10.1007/s10346-017-0883-y>, 2018.
- Miao, F., Xie, X., Wu, Y., and Zhao, F.: Data mining and deep learning for predicting the displacement of “step-like” landslides, *Sensors*, 22, 481, <https://doi.org/10.3390/s22020481>, 2022.
- Miralles, D. G., Holmes, T. R. H., De Jeu, R. A. M., Gash, J. H., Meesters, A. G. C. A., and Dolman, A. J.: Global land-surface evaporation
725 estimated from satellite-based observations, *Hydrology and Earth System Sciences*, 15, 453–469, <https://doi.org/10.5194/hess-15-453-2011>, 2011.
- Neaupane, K. and Achet, S.: Use of backpropagation neural network for landslide monitoring: a case study in the higher Himalaya, *Engineering Geology*, 74, 213–226, <https://doi.org/10.1016/j.enggeo.2004.03.010>, 2004.
- Nie, W., Krautblatter, M., Leith, K., Thuro, K., and Festl, J.: A modified tank model including snowmelt and infiltration time lags for
730 deep-seated landslides in alpine environments (Aggenalm, Germany), *Natural Hazards and Earth System Sciences*, 17, 1595–1610, <https://doi.org/10.5194/nhess-17-1595-2017>, 2017.
- Novellino, A., Cesarano, M., Cappelletti, P., Di Martire, D., Di Napoli, M., Ramondini, M., Sowter, A., and Calcaterra, D.: Slow-moving landslide risk assessment combining machine learning and InSAR techniques, *CATENA*, 203, 105 317, <https://doi.org/10.1016/j.catena.2021.105317>, 2021.
- 735 Parajka, J., Kohnová, S., Merz, R., Szolgay, J., Hlavčová, K., and Blöschl, G.: Comparative analysis of the seasonality of hydrological characteristics in Slovakia and Austria, *Hydrological Sciences Journal*, 54, 456–473, <https://doi.org/10.1623/hysj.54.3.456>, 2009.
- Pfeiffer, J., Zieher, T., Schmieder, J., Rutzinger, M., and Strasser, U.: Spatio-temporal assessment of the hydrological drivers of an active deep-seated gravitational slope deformation: the Vögelsberg landslide in Tyrol (Austria), *Earth Surface Processes and Landforms*, pp. 1–17, <https://doi.org/10.1002/esp.5129>, 2021.
- 740 Reichle, R., De Lannoy, G., Koster, R., Crow, W., Kimball, J., and Liu, Q.: SMAP L4 global 3-hourly 9 km EASE-grid surface and root zone soil moisture. Geophysical data, version 6, <https://doi.org/10.5067/08S1A6811J0U>, type: dataset, 2022.
- Ren, F., Wu, X., Zhang, K., and Niu, R.: Application of wavelet analysis and a particle swarm-optimized support vector machine to predict the displacement of the Shuping landslide in the Three Gorges, China, *Environmental Earth Sciences*, 73, 4791–4804, <https://doi.org/10.1007/s12665-014-3764-x>, 2015.
- 745 Stanley, T. A., Kirschbaum, D. B., Benz, G., Emberson, R. A., Amatya, P. M., Medwedeff, W., and Clark, M. K.: Data-driven landslide nowcasting at the global scale, *Frontiers in Earth Science*, 9, 378, <https://doi.org/10.3389/feart.2021.640043>, 2021.
- TensorFlow Developers: TensorFlow, <https://doi.org/10.5281/ZENODO.4724125>, 2022.
- Thomas, M. A., Collins, B. D., and Mirus, B. B.: Assessing the feasibility of satellite-based thresholds for hydrologically driven landsliding, *Water Resources Research*, <https://doi.org/10.1029/2019WR025577>, 2019.
- 750 van Asch, T., van Beek, L., and Bogaard, T.: Problems in predicting the mobility of slow-moving landslides, *Engineering Geology*, 91, 46–55, <https://doi.org/10.1016/j.enggeo.2006.12.012>, 2007.

- van Natijne, A., Bogaard, T., van Leijen, F., Hanssen, R., and Lindenbergh, R.: World-wide InSAR sensitivity index for landslide deformation tracking, *International Journal of Applied Earth Observation and Geoinformation*, 111, 102 829, <https://doi.org/10.1016/j.jag.2022.102829>, 2022.
- 755 van Natijne, A. L., Lindenbergh, R. C., and Bogaard, T. A.: Machine Learning: new potential for local and regional deep-seated landslide nowcasting, *Sensors*, 20, 1425, <https://doi.org/10.3390/s20051425>, 2020.
- Wang, Y., Tang, H., Wen, T., Ma, J., Zou, Z., and Xiong, C.: Point and interval predictions for Tanjiahe landslide displacement in the Three Gorges reservoir area, China, *Geofluids*, 2019, 1–14, <https://doi.org/10.1155/2019/8985325>, 2019.
- Wen, T., Tang, H., Wang, Y., Lin, C., and Xiong, C.: Landslide displacement prediction using the GA-LSSVM model and time series analysis: a case study of Three Gorges Reservoir, China, *Natural Hazards and Earth System Sciences*, 17, 2181–2198, <https://doi.org/10.5194/nhess-17-2181-2017>, 2017.
- 760 World Meteorological Organization (WMO): WMO atlas of mortality and economic losses from weather, climate and water extremes (1970–2019) (WMO-no. 1267), Tech. Rep. 1267, WMO, Geneva, https://library.wmo.int/index.php?lvl=notice_display&id=21930#.YS9CMNMzZBx, 2021.
- 765 Xie, P., Zhou, A., and Chai, B.: The application of Long Short-Term Memory (LSTM) method on displacement prediction of multifactor-induced landslides, *IEEE Access*, 7, 54 305–54 311, <https://doi.org/10.1109/ACCESS.2019.2912419>, 2019.
- Yang, B., Yin, K., Lacasse, S., and Liu, Z.: Time series analysis and long short-term memory neural network to predict landslide displacement, *Landslides*, <https://doi.org/10.1007/s10346-018-01127-x>, 2019.
- Yatheendradas, S., Kirschbaum, D., Nearing, G., Vrugt, J. A., Baum, R. L., Wooten, R., Lu, N., and Godt, J. W.: Bayesian analysis of the impact of rainfall data product on simulated slope failure for North Carolina locations, *Computational Geosciences*, <https://doi.org/10.1007/s10596-018-9804-y>, 2019.
- 770 Zhang, X., Zhu, C., He, M., Dong, M., Zhang, G., and Zhang, F.: Failure mechanism and long short-term memory neural network model for landslide risk prediction, *Remote Sensing*, 14, 166, <https://doi.org/10.3390/rs14010166>, 2021.
- Zhou, C., Yin, K., Cao, Y., and Ahmed, B.: Application of time series analysis and PSO–SVM model in predicting the Bazimen landslide in the Three Gorges Reservoir, China, *Engineering Geology*, 204, 108–120, <https://doi.org/10.1016/j.enggeo.2016.02.009>, 2016.
- 775 Zhu, X., Xu, Q., Tang, M., Nie, W., Ma, S., and Xu, Z.: Comparison of two optimized machine learning models for predicting displacement of rainfall-induced landslide: A case study in Sichuan Province, China, *Engineering Geology*, 218, 213–222, <https://doi.org/10.1016/j.enggeo.2017.01.022>, 2017.
- Zhu, Z., Wulder, M. A., Roy, D. P., Woodcock, C. E., Hansen, M. C., Radeloff, V. C., Healey, S. P., Schaaf, C., Hostert, P., Strobl, P., Pekel, J.-F., Lymburner, L., Pahlevan, N., and Scambos, T. A.: Benefits of the free and open Landsat data policy, *Remote Sensing of Environment*, 224, 382–385, <https://doi.org/10.1016/j.rse.2019.02.016>, 2019.
- 780 Zieher, T., Pfeiffer, J., van Natijne, A., and Lindenbergh, R.: Integrated monitoring of a slowly moving landslide based on total station measurements, multi-temporal terrestrial laser scanning and space-borne interferometric synthetic aperture radar, in: 2021 IEEE International Geoscience and Remote Sensing Symposium IGARSS, pp. 942–945, IEEE, Brussels, Belgium, <https://doi.org/10.1109/IGARSS47720.2021.9553324>, iSSN: 2153-7003, 2021.
- 785